Bioactive Materials 34 (2024) 80–97

Contents lists available at ScienceDirect

Bioactive Materials

journal homepage: www.keaipublishing.com/en/journals/bioactive-materials

A micro-fragmented collagen gel as a cell-assembling platform for critical limb ischemia repair

Haeun Chung [a,b], Jung-Kyun Choi [a,b], Changgi Hong [c,d], Youngseop Lee [c], Ki Hyun Hong [a,1], Seung Ja Oh [e], Jeongmin Kim [c,d], Soo-Chang Song [a,b], Jong-Wan Kim [f], Sang-Heon Kim [a,b,*]

[a] Center for Biomaterials, Biomedical Research Institute, Korea Institute of Science and Technology (KIST), Seoul, 02792, Republic of Korea
[b] Division of Bio-Medical Science and Technology, KIST School, University of Science and Technology, Seoul, 02792, Republic of Korea
[c] Department of Applied Bioengineering, Graduate School of Convergence Science and Technology, Seoul National University, Seoul, 08826, Republic of Korea
[d] Research Institute for Convergence Science, Seoul National University, Seoul, 08826, Republic of Korea
[e] Department of Genetics and Biotechnology, College of Life Sciences, Kyung Hee University, Yongin-si, Gyeonggi-do, 17104, Republic of Korea
[f] S.Biomedics Co., Ltd., Seoul, 04797, Republic of Korea

ARTICLE INFO

Keywords:
Regenerative medicine
Stem cell therapy
Collagen microgel
3D cell culture
Critical limb ischemia

ABSTRACT

Critical limb ischemia (CLI) is a devastating disease characterized by the progressive blockage of blood vessels. Although the paracrine effect of growth factors in stem cell therapy made it a promising angiogenic therapy for CLI, poor cell survival in the harsh ischemic microenvironment limited its efficacy. Thus, an imperative need exists for a stem-cell delivery method that enhances cell survival. Here, a collagen microgel (CMG) cell-delivery scaffold (40 × 20 μm) was fabricated via micro-fragmentation from collagen–hyaluronic acid polyionic complex to improve transplantation efficiency. Culturing human adipose-derived stem cells (hASCs) with CMG enabled integrin receptors to interact with CMG to form injectable 3-dimensional constructs (CMG-hASCs) with a microporous microarchitecture and enhanced mass transfer. CMG-hASCs exhibited higher cell survival ($p < 0.0001$) and angiogenic potential in tube formation and aortic ring angiogenesis assays than cell aggregates. Injection of CMG-hASCs intramuscularly into CLI mice increased blood perfusion and limb salvage ratios by 40 % and 60 %, respectively, compared to cell aggregate-treated mice. Further immunofluorescent analysis revealed that transplanted CMG-hASCs have greater muscle regenerative and angiogenic potential, with enhanced cell survival than cell aggregates ($p < 0.05$). Collectively, we propose CMG as a cell-assembling platform and CMG-hASCs as promising therapeutics to treat CLI.

1. Introduction

Critical limb ischemia (CLI) is the most severe form of peripheral arterial disease that manifests as atherosclerosis [1]. The current primary treatment option for CLI is surgical revascularization, but up to 40 % of patients with CLI eventually end up with amputation [1]. Therefore, alternative therapy for CLI is urgently needed and has led to a search for effective angiogenic therapeutics. Angiogenesis is a complex, yet organized process that requires the sequential release of a series of growth factors and cytokines at different time points to initiate a balanced angiogenic cascade [2]. As a result, stem cell therapy using mesenchymal stem cells (MSCs) has emerged as a promising therapeutic option for CLI, as it can secrete a plethora of paracrine factors to orchestrate complex angiogenic processes. Human adipose-derived stem cells (hASCs) have gained popularity as they can be harvested with high yield through minimally invasive methods, involve simple isolation procedures with relatively short doubling time for fast expansion, and are immune-privileged cells that possess superior angiogenic potential, capable of secreting multiple angiogenic factors at therapeutic concentrations, making hASCs an attractive cell type for the treatment of CLI [1,3,4].

Despite the promising therapeutic effects of stem cells, as observed in both preclinical and clinical studies, the use of MSCs in regenerative medicine has been limited by the extremely low survival rate of transplanted cells and their poor engraftment into the host. Previous studies

Peer review under responsibility of KeAi Communications Co., Ltd.
* Corresponding author. Korea Institute of Science and Technology, Seoul, 02792, Republic of Korea.
E-mail address: skimbrc@kist.re.kr (S.-H. Kim).
[1] Present Address: NTIS Team, Center for Standardization Planning, IRIS Working Group, Korea Institute of S&T Evaluation and Planning

https://doi.org/10.1016/j.bioactmat.2023.12.008
Received 31 July 2023; Received in revised form 25 November 2023; Accepted 7 December 2023

Abbreviations

2-NBDG	2-(N-(7-nitrobenz-2-oxa-1,3-diazol-4-yl)amino)-2-deoxyglucose
3D	3-dimensional
BSA	bovine serum albumin
CLI	critical limb ischemia
CMG	collagen microgel
DAPI	4′,6-diamidino-2-phenylindole
EBM	endothelial basal medium
ECM	extracellular matrix
EGM	endothelial growth medium
ERK	extracellular signal-regulated kinase
FAK	focal adhesion kinase
HA	hyaluronic acid
H&E	hematoxylin & eosin
hASCs	human adipose-derived stem cells
HIF-1α	hypoxia-inducible factor-1α
HNA	human nuclear antigen
HUVECs	human umbilical vein endothelial cells
MT	masson's trichrome
MSCs	mesenchymal stem cells
PBS	phosphate-buffered saline
RhoA	ras homolog family member A
ROCK	rho-associated coiled-coil kinase
SD	standard deviation
SEM	scanning electron microscopy
SFM	serum-free medium

have reported that up to 99 % of the injected cells die from apoptosis and necrosis within the first few hours after transplantation, due to the harsh environment at the injury site such as loss of anchorage site, hypoxia, nutritional stress, and host immune response [5]. Three-dimensional constructs, such as cell spheroids and cell-scaffold composites, are being employed to increase transplanted cell survival and enhance therapeutic efficacy by enhancing the secretion of angiogenic, anti-inflammatory, immunomodulatory, and survival factors [6–8]. Although cell spheroids offer benefits such as enhanced cell survival and increased secretion of paracrine factors via intrinsic hypoxia and cell-to-cell interaction, they lack cell-to-ECM interaction and exhibit very restricted mass transfer, eventually inducing apoptosis and formation of necrotic core [8]. An alternative strategy to improve cell survival is to use hydrogels as scaffolds, as they can mimic extracellular matrix (ECM) and display mechanical properties similar to those of numerous soft tissues [9]. The scaffold can serve as a surface for the attachment of anchorage-dependent cells to prevent anoikis before transplantation while it can act as a physical barrier against immune cells, protecting cells from inflammatory cell attack and promoting the long-term secretion of paracrine factors from MSCs after transplantation [10,11]. However, the use of scaffold makes it difficult to achieve homogeneous cell distribution, and the initial cell density tends to be low, requiring a large volume to be injected to transplant a large number of cells, eventually leading to a large surgical wound and long post-operative recovery time [12,13].

Given the advantages and disadvantages of both cell spheroids and the use of scaffolds, microgel assembly appears to be an intriguing hybrid where cells are assembled using microgel as scaffolds to form a larger 3D construct. Advantages of this bottom-up tissue engineering technology include the injectability owing to their small size, the simplicity of achieving uniform cell distribution, and an increased porosity created by the interspace between microgels [14]. Compared to cell spheroids that lack porosity and nanoporous bulk hydrogels, microgel assemblies inherently form micropores within their microstructure, allowing enhanced mass transfer within 3D constructs [15,16]. Moreover, in contrast to the conventional bulk hydrogel where infiltration of host cells is limited due to small pores within the dense fibrillar network, the inherent microporosity of microgel assembly facilitates infiltration of host cells and blood vessels, allowing tissue repair to commence before biodegradation occurs, promoting a faster regeneration of injured tissue [17]. Therefore, the use of microgel as a scaffold not only facilitates cell adhesion prior to transplantation but also promotes cell survival after transplantation by protecting cells from the host immune system and promoting enhanced mass transfer.

Microgels fabricated using polyethylene glycol, hyaluronic acid, gelatin, gelatin methacrylate, or alginate using fabrication technologies such as microfluidics, emulsion, lithography, spraying, and mechanical fragmentation have been applied to tissue engineering [14]. The assembly of these microgels often involved chemically modified cross-linkers or photo-polymerization for intra-microgel crosslinking [18–22]. Although these methods can offer benefits such as a rapid cross-linking rate, the ability to incorporate bioactive molecules, and the fine-tunability of porosity and mechanical properties of the resulting microgel assembly, adding functional moieties to microgel may require a complicated synthesis procedure and may potentially cause cytotoxicity during cross-linking. Thus, a more practical approach to fabricating microgel and a cytocompatible approach to forming microgel assembly is desired.

Type I collagen-based microgels are extremely appropriate as a 3D scaffold material because of their self-assembly into a fibrillary gel, the absence of antigenicity, their bioactivity, and the wide availability of collagen in the native ECM. In particular, collagen has been approved by the U.S. Food and Drug Administration for its long history of use as a medical device such as dermal fillers owing to its excellent safety profile, making it an ideal biomaterial of choice for implantation [23]. Additionally, collagen serves as a natural ligand for integrin receptors on the cell membrane, allowing cells to biologically cross-link CMG to form 3D constructs, which does not require extensive fabrication procedure to add crosslinkers and therefore poses no risk of cytotoxicity to cells. Several studies also used collagen- or gelatin-based microgels to deliver cells to the injury site, but mainly by encapsulating cells within the microgel [24–26]. This method may be advantageous in protecting cells from external injection force and the host's immune system; however, it is subject to low cargo loading efficiency due to the restricted microgel size, and it may not be suitable for delivery by minimally invasive method, as the size of these microgels typically spanned over a few hundred micrometers.

This study presents a simple, cost-effective, and cytocompatible approach for the fabrication of collagen microgel (CMG) with dimensions of approximately 40 μm in length and 20 μm in width, which is a size that is acceptable for delivery using a minimally invasive method. Our CMG platform showed promising possibilities as a cell-carrying platform that promoted increased porosity, enhanced mass transfer, and high cell viability. The increased angiogenic function of the CMG-hASCs was demonstrated *in vitro* and *in vivo*, which strongly suggested CMG-hASCs as a potential therapeutic for CLI treatment.

2. Materials and methods

2.1. Fabrication of collagen/HA microgel

Stock solutions of 25 % (w/w) atelocollagen (MSBio, Inc., Seoul, South Korea) and 10 % (w/w) sodium hyaluronate (HA) (Contipro Inc., Dolní Dobrouč, Czech Republic) were prepared by dissolving atelocollagen in 0.01 N hydrochloric acid and HA in phosphate-buffered saline (PBS). Collagen and HA were added to a tube and mixed with a

spatula while on ice. The pH of the mixture was adjusted to pH 7.1–7.3, by adding 2 N NaOH or 1 N HCl. To achieve the desired final volume, PBS was added, and the mixture was incubated at 37 °C for at least 30 min for gelation. The collagen/HA gel was added to a new tube containing StemPro™ serum-free medium (SFM, Gibco, Waltham, MA, USA) and glass beads. The gel was broken into microgel by giving agitation at 1500 opm for 30 s using a bead beater (Mini-Beadbeater-24, BioSpec Products, Bartlesville, OK, USA). The resulting CMG solution was vacuum-filtered using a 100-μm filter and stored at 25 ± 2 °C until use.

2.2. Characterization of collagen/HA hydrogel and CMG

2.2.1. Zeta potential of CMG

Hydrogels containing varying concentrations of collagen and HA were prepared and broken in distilled water that was pre-set to pH values of 3–11. The surface charge of the CMG was determined by measuring the zeta potential of the microgel using a Zetasizer Nano ZS system (Malvern Panalytical Ltd., Nottingham, UK).

2.2.2. Scanning electron microscopy

Samples were fixed with 2.5 % glutaraldehyde for primary fixation (Sigma-Aldrich, St. Louis, MO, USA) for 2 h and then with 2 % osmium tetroxide (Sigma-Aldrich) for secondary fixation for 3 h at 25 ± 2 °C. The fixed samples were washed with distilled water and dehydrated with increasing concentrations of ethanol (30 %, 50 %, 70 %, 80 %, 90 %, and 100 %) for 5 min each at 25 ± 2 °C. Hexamethyldisilazane (Sigma-Aldrich) was added, and the samples were dried overnight in a vacuum chamber at 25 ± 2 °C. The samples were placed on SEM stubs and sputter-coated with platinum for 60 s each in an upright position and on each side. Images of the prepared samples were captured using a field-emission SEM (Inspect F50, FEI Company, Hillsboro, OR, USA).

2.2.3. 3D stochastic optical reconstruction microscopy (STORM) imaging

The thickness of collagen fibers of CMG was analyzed using 3D stochastic optical reconstruction microscopy (STORM). The CMG was first conjugated to Alexa Fluor™ 647 by incubating with NHS-ester-Alexa-647 at 5 μg/mL for 1 h at 25 ± 2 °C. CMG was then washed in PBS to get rid of unbound dye, placed on #1.5H coverslips pre-coated with 0.5 % of 3-aminopropyltriethoxysilane and mounted with a STORM imaging buffer (100 mM cysteamine, 10 % glucose, 0.8 mg/mL glucose oxidase, 40 μg/ml catalase, 50 mM Tris-HCl, and 10 mM NaCl in PBS, pH 8.0). The samples were subsequently sealed with nail polish prior to imaging. The prepared sample was loaded onto a home-built STORM setup (objective lens: 100 × /1.45), as detailed by Lee et al., which captures the astigmatic point spread functions of Alexa Fluor™ 647 molecules for 3D localization [27]. Single-molecule videos of the CMG were acquired at a rate of 50 frames/s over 20,000 image frames, using a 642 nm laser for excitation (average illumination intensity: ~10 kW/cm^2) together with a weak 405 nm laser activation. The STORM video data were then localized, and 3D STORM images were reconstructed following the methodology described by Lee et al. [27]. The lateral and axial cross-sectional intensity profiles of 10 random fibers within the image were analyzed, and the cross-sectional thickness was determined from the full width at half-maximum intensity of these profiles.

2.2.4. Size distribution of CMG

The size distribution of the CMG was analyzed using an automated Mophologi G3 optical microscope (Malvern Panalytical Ltd.). Briefly, microgels were dispersed in distilled water on a glass slide, covered with a cover slip, and scanned using an automated microscope to capture images of the CMG. The images were analyzed using a computer equipped with Morphologi software (Malvern Panalytical Ltd.).

2.3. CMG as a stem cell carrier

Human adipose-derived stem cells (hASCs) were obtained from S. Biomedics (Seoul, South Korea) and were determined to meet the minimal criteria set out by the International Society for Cell Therapy. The hASCs were expanded to the fifth passage in CEFOgro medium (CEFO Co., Seoul, South Korea) in a humidified chamber set to 37 °C and 5 % CO_2. To prepare the 3D constructs, hASCs were trypsinized, resuspended in SFM, and seeded into 96-well round-bottom ultra-low attachment plates at 2 × 10^5 cells per well. The prepared CMG solution was added to each well at a 1:0, 1:1, 1:2, or 1:4 ratio (cell:CMG ratio as predetermined by pelleted volume), and SFM was added to make up a total volume of 300 μL per well. The resulting cell–CMG culture was mixed well by pipetting and kept in an incubator at 37 °C for 24 h to form 3D constructs.

2.4. Rheological properties of 3D constructs

To form 3D constructs of approximately 500 μL in volume, 8 × 10^6 cells, 4 × 10^6 cells, or 2 × 10^6 cells were mixed with CMG at a 1:1, 1:2, or 1:4 ratio, respectively, in non-tissue cultured 24-well plates and incubated at 37 °C for 24 h. The storage (G') and loss (G'') moduli were measured to assess the viscoelastic properties of the 3D constructs using an MCR 102 rheometer (Anton-Paar, Graz, Austria). Dynamic time sweeps were performed at a frequency of 10 rad/s and 0.5 % strain at 25 °C until a plateau was reached.

2.5. Function-blocking assay

To block the functions of CD44 or integrin β1 receptors prior to the formation of 3D constructs, harvested cells were pre-incubated with rat anti-CD44 (Hermes-1, Invitrogen, Waltham, MA, USA) at 0, 10, 30, or 50 μg/mL or rat anti-human CD29 (integrin β1, BD Biosciences, Franklin Lakes, NJ, USA) at 0, 5, 10, or 20 μg/mL for 30 min in a 37 °C incubator. They were then mixed with CMG at a 1:0, 1:1, 1:2, or 1:4 ratio and incubated at 37 °C for 24 h to form the 3D constructs. For inhibitor treatment, the cells were trypsinized, harvested, and treated at 0, 10, 30, or 50 μM with DMSO or inhibitors of focal adhesion kinase (FAK; PF-573228), Rho-associated coiled-coil kinase (ROCK; Y-27632), and myosin (blebbistatin). They were then mixed with CMG at a 1:0, 1:1, 1:2, or 1:4 ratio and incubated at 37 °C for 24 h to form 3D constructs. As a negative control, 50 μM extracellular signal-regulated kinase inhibitor (ERK; U0126) was used. The inhibition of 3D cell formation was determined by measuring the diameter of the final 3D construct. Viability was assessed using the trypan blue exclusion assay.

2.6. Characterization of 3D constructs

2.6.1. Micro-CT

The porosity of the 3D constructs was analyzed using micro-CT. Briefly, the samples were fixed in 4 % paraformaldehyde and stained with 5 % phosphotungstic acid in 70 % ethanol for 3 d. The prepared samples were then placed in a tube containing PBS, and computerized tomography scans were taken using a micro-CT (Skyscan 1172, Bruker, Billerica, MA, USA) with the following parameters: aluminum filter, 0.5 mm; X-ray tube voltage, 75 kV; tube current, 134 μA; pixel size, 2.6 μm, and scanning angle range, 360°. The data were reconstructed using NRecon software (Bruker) and analyzed using CTAn software (Bruker).

2.6.2. Glucose uptake assay

A glucose uptake assay was used to assess the mass transfer of the 3D constructs. Samples were incubated in 500 μM 2-(N-(7-nitrobenz-2-oxa-1,3-diazol-4-yl)amino)-2-deoxyglucose (2-NBDG) for 1 h and snap-frozen in liquid nitrogen. Cryosections (10-μm thick) were washed in PBS for 30 s and mounted in a mounting medium containing 4′,6-diamidino-2-phenylindole (DAPI). The sections were visualized under an

LSM 700 confocal microscope (Zeiss, Oberkochen, Germany).

2.6.3. Hypoxia

The 3D constructs were prepared as described above and incubated with 10 mM pimonidazole (Hypoxyprobe, Burlington, MA, USA) for 5 h. Samples were prepared as frozen blocks for immunofluorescent staining of pimonidazole or cell lysates, followed by quantification using western blotting.

2.7. Immunofluorescence staining

For immunofluorescence staining of the 3D constructs, the samples were prepared as frozen blocks and cut into 10-μm-thick sections. For immunofluorescence staining of thigh muscle tissues, the samples were prepared as paraffin blocks and cut into 4-μm-thick sections. The prepared sections were blocked in blocking solution [2 % bovine serum albumin (BSA) + 0.1 % Triton X-100 in PBS] for 1 h. The sections were incubated with primary antibodies (diluted with blocking solution) overnight at 4 °C and subsequently with fluorescence-conjugated secondary antibodies (diluted with blocking solution at 1:500) for 1 h at 25 ± 2 °C. The samples were then mounted using Vectashield antifade mounting medium containing DAPI (Vector Laboratories Inc., Newark, CA, USA), and fluorescent images were captured using a Zeiss LSM 700 confocal microscope (Zeiss). Antibody information is provided in Supplementary Table S1.

2.8. Western blot

Cell lysates were prepared via homogenization using a Mini-Beadbeater-24 (Biospec Products) in 20 mM Tris-HCl buffer (pH 7.2) containing a protease and phosphatase inhibitor cocktail. Cell debris and CMG were removed via centrifugation. Protein was separated via electrophoresis on 4–15 % gradient gel (Bio-Rad Laboratories, Hercules, CA, USA) and transferred to polyvinylidene fluoride membranes (Millipore, Burlington, MA, USA). The membranes were blocked with 5 % BSA in TBST (1 M Tris-HCl, pH 7.4, 0.9 % NaCl, and 0.05 % Tween-20) for 1 h and probed with primary antibody, diluted with 1 % BSA in TBST, with rocking overnight at 4 °C. The membranes were washed three times in TBST and incubated in HRP-conjugated secondary antibody at a 1:2000 dilution for 2 h. The western blots were visualized with an enhanced chemiluminescence system, and images were captured with an iBright CL1500 imaging system (Thermo Fisher Scientific). Antibody information is provided in Supplementary Table S1.

2.9. Assessment of cell viability of 3D constructs

To determine cell viability, the 3D constructs were stained with 20 μM of live (calcein AM) and 10 μM of dead (propidium iodide) dyes at 37 °C for 5 h. Samples were frozen in optimal cutting temperature compound and 10 μm-thick cryosections were prepared, mounted, and covered with a cover slip. Fluorescence images were captured using an LSM 700 confocal microscope (Zeiss).

2.10. RNA sequencing analysis

RNA sequencing analysis was performed on hASCs cultured on non-tissue culture plates and 3D constructs cultured with CMG at ratios of 1:0 and 1:4 for 24 h. Total mRNA was extracted using the TRIzol method and its quality was assessed using an Agilent 2100 bioanalyzer (Agilent Technologies, Santa Clara, CA, USA), and the cDNA library was constructed using the QuantSeq 3′ mRNA-Seq Library Prep Kit (Lexogen Inc., Wien, Austria), following the manufacturer's instructions. High-throughput sequencing was performed using NextSeq 500 (Illumina, San Diego, CA, USA). The sequenced QuantSeq 3′ mRNA-Seq reads were aligned using Bowtie2. The differentially expressed genes were determined based on a fold change ≥1.5 and a p-value <0.05 [26]. Gene classification was based on searches performed using DAVID and Medline search engines.

2.11. In vitro tube formation assay

Green fluorescent protein-tagged human umbilical vein endothelial cells (HUVECs) were cultured in endothelial growth medium (EGM)-2 (Lonza, Basel, Switzerland) supplemented with supplements and antibiotics until passage four. For the tube formation assay, 24-well transwell culture plates (SPL Life Sciences, Pocheon, South Korea) were coated with growth factor reduced-basement membrane extract (Matrigel®, Corning, Corning, NY, USA) and incubated at 37 °C for 40 min. Serum-starved HUVECs were seeded at a density of 1×10^5 cells per well in the lower compartment of transwell plates and incubated for 40 min at 37 °C in an incubator. Then, (1) positive control, (2) negative control, (3) CMG, (4) 1:0 (cells:CMG), (5) 1:1, (6) 1:2, or (7) 1:4 was placed in the upper compartment of transwell plates and co-cultured with HUVECs for 16 h. All experimental groups, except for the positive and negative controls, were cultured in SFM. The positive control was cultured in EGM supplemented with angiogenic growth factors, and the negative control was cultured in endothelial basal medium (EBM) with no additional supplements. The CMG group involved co-culturing HUVECs with CMG and was included to determine the effect of CMG alone. Tube formation in the wells was visualized using confocal microscopy.

2.12. CLI model

2.12.1. Animal care

The animals were handled in compliance with the guidelines set by the National Institutes of Health of South Korea. Thirty male BALB/c *nu/nu* mice (5-weeks-old) were purchased from Orient Bio Inc. (Seongnam, South Korea). Five mice were used for the *ex vivo* mouse aortic ring assay and 25 were used to induce CLI. All mice were given *ad libitum* access to food and water and allowed to acclimatize for at least 1 week. Throughout the study, mice were housed in a room maintained at 24 °C and 60 % humidity, with a 12-h light/dark cycle. All procedures involving animals were approved by the International Animal Care and Use Committee of the Korea Institute of Science and Technology [KIST-2021-090].

2.12.2. Ex vivo mouse aortic ring assay

Immediately following euthanasia by cervical dislocation, the thoracic cavity of mice (6-weeks-old) was opened, the thoracic aorta was harvested, and its fibro-adipose tissue was carefully removed. The aortic tissue was cut sagittally into 1-mm aortic rings and subjected to overnight serum starvation. For the *ex vivo* mouse aortic ring assay, aortic rings were embedded in 1 % rat tail collagen gel (Corning) in the lower compartment of pre-chilled 24-well Transwell culture plates (SPL Life Sciences) and cultured for 7 d under seven different conditions: (1) positive control, (2) negative control, (3) CMG, (4) 1:0, (5) 1:1, (6) 1:2, or (7) 1:4 in the upper compartment of the cell inserts. All experimental groups, except for the positive and negative controls, were cultured in SFM. The positive control was cultured in EGM supplemented with angiogenic growth factors, and the negative control was cultured in EBM. The aortic rings were co-cultured for 7 d at 37 °C and 5 % CO_2, and the media was changed daily. For selective visualization of sprouting vessels, aortic rings were fixed in 4 % PFA, blocked (1 % BSA + 0.5 % Triton X-100), and stained with an endothelial cell marker, isolectin IB4 conjugated Alexa Fluor™ 488 (Invitrogen). Images were acquired using a fluorescence microscope (Zeiss). To quantify the outgrowth of microvessels, images were analyzed using ImageJ software (ImageJ, Bethesda, MD, USA).

2.12.3. Induction of CLI

Twenty-five six-week-old male BALB/c *nu/nu* mice were

anesthetized via isoflurane inhalation. To induce ischemia, the skin on the right hindlimb of each mouse was excised to expose the femoral artery, and the femoral artery was ligated with a 5-0 black silk suture (AILEE Co. Ltd., Busan, South Korea) at the proximal branch of the external iliac artery and at the distal point where it bifurcated into the saphenous and popliteal arteries. The ligated femoral artery was excised and the incision on the skin was sutured. Blood flow blockade was monitored by Laser Doppler Perfusion Imaging (Moor Instruments Ltd., Devon, UK). The mice were randomly divided into five groups (n = 5 per group) and given five different treatments 1 d after surgery: (1) PBS as a negative control, (2) CMG, (3) CMG/hASCs (2×10^5 cells/mouse) suspension, (4) cell aggregates, and (5) CMG-hASCs construct. To eliminate the possible effect caused by volume difference, the treatments were loaded with PBS to a final volume of 100 μL into low dead volume syringes equipped with 24-gauge needles (Kovax-Needle, Korea Vaccine, Ansan, South Korea) and administered intramuscularly into the medial thigh of the ischemic limb. The morphology and recovery of blood flow in the ischemic limbs were monitored using Laser Doppler Perfusion Imaging once a week for up to 28 d.

2.12.4. *In vitro and in vivo biodegradation assay*

To determine the *in vitro* enzymatic biodegradation rate, CMG or 3D constructs prepared at 1:1, 1:2 and 1:4 ratio was lyophilized and treated with 30U collagenase and 10U hyaluronidase in 1 mL of PBS at 37 °C. The biodegradation ratios were calculated by dividing the weight at specific time points by the initial weight at 0 h multiplied by 100. To determine the *in vivo* biodegradation rate, CMG conjugated to atto-488-NHS was injected into normal and ischemic limbs, and its fluorescent intensities were measured using an *in vivo* imaging system (IVIS, PerkinElmer, Waltham, MA, USA). The biodegradation rate was calculated by normalizing the fluorescence intensity to the value of 0 d.

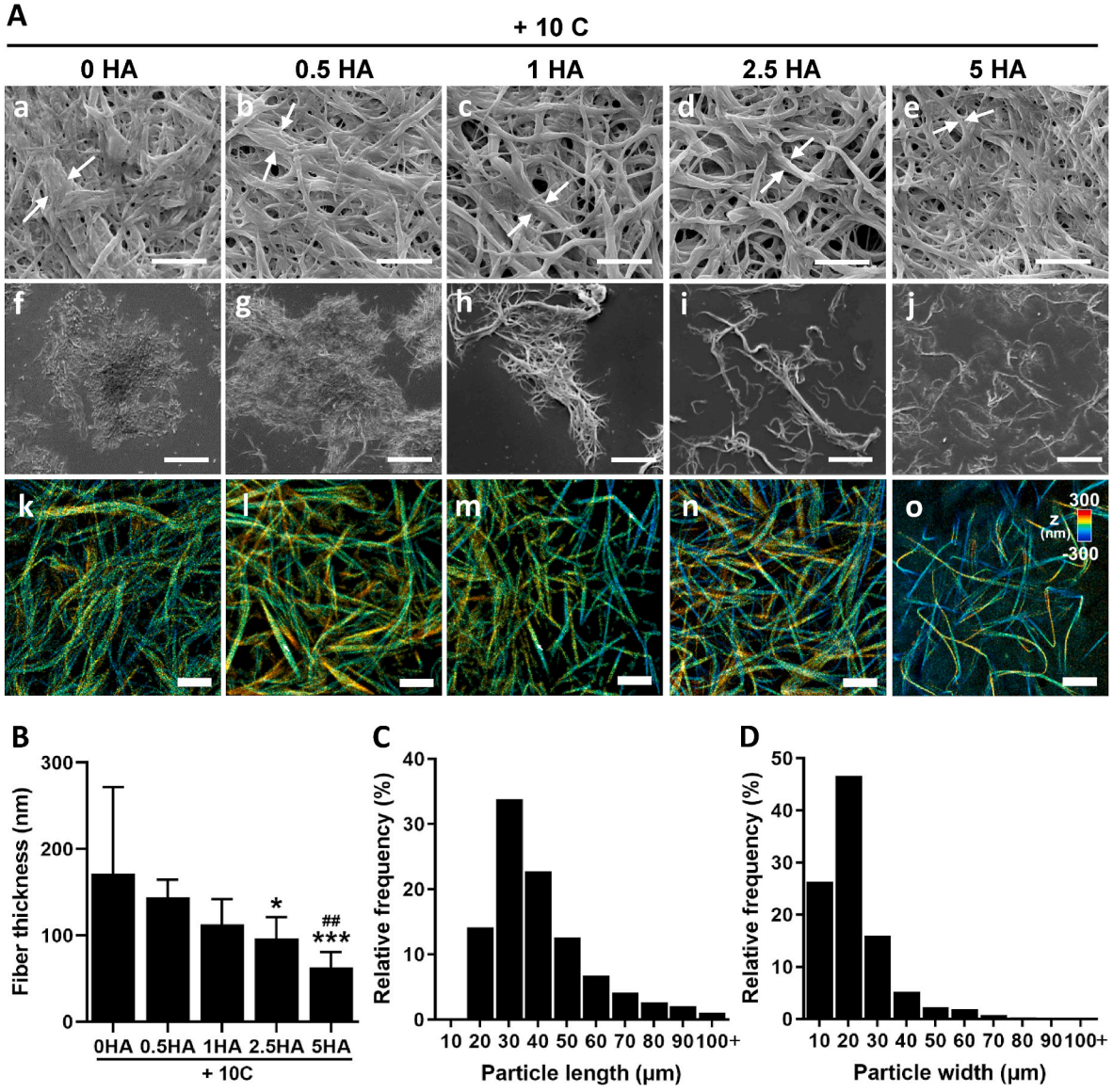

Fig. 1. Effect of varying HA concentration on collagen fibrillogenesis. (A) SEM images showing the morphology of hydrogels (a–e) and microgels (f–j) and 3D super-resolution STORM images showing microgels (k–o) consisting of 10 % collagen plus 0 %, 0.5 %, 1 %, 2.5 %, or 5 % HA. The thickness of representative collagen fibers is indicated with arrows. Scale bars in panels a–e represent 2.5 μm, in panels f–j represent 20 μm and in panels k–o represent 2.5 μm. (B) Quantification of fiber thickness of microgels as analyzed using 3D super-resolution STORM images. n = 10 per group. Data are presented as mean ± SD. One-way ANOVA with multiple comparison tests. *p < 0.05, ***p < 0.001 against the 0 % HA group. ##p < 0.01 against the 0.5 % HA group. (C–D) Frequency size distribution of microgels according to length and width, as determined using Morphologi G3.

2.13. Statistical analysis

All statistical analyses were performed using Prism 7 software (GraphPad, San Diego, CA, USA). Comparisons between multiple experimental groups were performed using one-way or two-way ANOVA, assuming a Gaussian distribution and equal standard deviation (SD), followed by multiple comparison tests with a confidence level of 95 %. Statistical significance was set at $p < 0.05$.

3. Results

3.1. Effect of HA on fibrillogenesis

To determine whether the collagen and HA were interacting electrostatically, we fabricated CMGs comprising varying concentrations of collagen (5 %–15 %) or HA (0 %–5 %) and measured zeta potential in aqueous solutions ranging from pH 3–11. The isoelectric point of the 10 % collagen gel was determined to be around 10.4. The addition of 0.5 % HA to the collagen shifted its isoelectric point to approximately 4.4, and it continued to decrease with increasing HA concentration and vice versa (Supp. Figs. S1A–B). This result indicates that, at physiological pH, the positively charged collagen interacted electrostatically with the negatively charged HA, forming a polyionic complex.

To determine the effect of HA on collagen fibrillogenesis, we mixed 10 % collagen gel with varying concentrations of HA (0%–5%) and examined the thickness of the resulting collagen fibers. As depicted by SEM images of hydrogel and 3D super-resolution STORM images of microgel (Fig. 1A and B), increasing HA concentration resulted in collagen fiber thinning. When mechanical stress was applied to the hydrogel, the bulk hydrogel fragmented into micro-sized gels, with the overall size decreasing with increasing HA concentration, presumably owing to HA-induced collagen fiber thinning (Fig. 1A). In contrast, when we mixed 2.5 % HA with varying concentrations of collagen (5%–15 %), we observed thicker collagen fibers and an increase in the overall size of microgel (Supp. Figs. S1C–D). Microgels fabricated with 10 % collagen and 5 % HA resulted in the smallest and most uniform distribution of microgel size and were manufactured in the highest yield (Fig. 1C and D, Supp. Figs. S1E–F). Microgels prepared under conditions of 10 % collagen and 5 % HA were used in this study.

3.2. hASCs assemble with CMG to form 3D constructs

Determination of the formation of 3D constructs was made by incubating fabricated CMG with hASCs at 1:0, 1:1, 1:2, 1:4, 1:8, and 1:16 ratios. Increasing the cell:CMG ratio from 1:1 to 1:16 resulted in the contraction of CMG by cells and hence the formation of 3D constructs; however, the degree of contraction decreased with increasing cell:CMG ratio (Supp. Fig. S2A). Furthermore, placing each group out from the medium revealed that 1:0, 1:1, 1:2, and 1:4 groups were able to maintain their integrity, whereas 1:8 and 1:16 groups failed to maintain their integrity and collapsed, presumably due to the lower packing density of CMG (Supp. Fig. S2B). To confirm the injectability of 3D constructs, each group was passed through a 24-gauge needle, and it was determined that all experimental groups were able to pass through the needle without affecting cell viability (Fig. 2A, Supp. Fig. S3A). Unlike the 3D constructs comprising hASCs and CMG, CMG alone exited the needle as droplets, indicating that the presence of hASCs was necessary to connect the microgels. Rheological measurements of the experimental groups indicated that when 0.5 % strain was applied, the mechanical properties of CMG alone were weak, with storage and loss moduli of around 100 Pa and 60 Pa, respectively; however, the incubation of hASCs with CMG increased its viscous and elastic properties, presumably owing to cells crosslinking with the microgel (Fig. 2B). The distribution of hASCs and CMG in the 3D constructs were observed through immunofluorescent and SEM images of cross-sections of the 3D constructs. The results revealed that the cells and CMG were uniformly distributed across the 3D constructs. Although the 1:0 group did not contain CMG, collagen type 1 was still observed, presumably because of collagen type 1 secreted from hASCs (Fig. 2C and D). Increasing the CMG ratio in the 3D constructs increased the distance between neighboring cells.

3.3. hASCs interact with CMG via integrin

CMG was observed to be assembled by hASCs into a 3D construct (Supp. Fig. S3B). To determine the mechanism of assembly of hASCs and CMG into 3D constructs, we used antibodies and inhibitors to block the signaling pathways involved in actin contraction. Because the fabricated CMG was comprised of HA and collagen, we blocked CD44 (HA receptor) or integrin β1 (collagen receptor) on the cell membranes by incubating the constructs with function-blocking antibodies and determined the effect of blocking these receptors on 3D formation. Although the collagen-binding receptors are integrins ($\alpha_1\beta_1$, $\alpha_2\beta_1$, $\alpha_{10}\beta_1$, and $\alpha_{11}\beta_1$), they all require the β1 subunit; therefore, using a function-blocking antibody specific to integrin β1 would be sufficient to block all four heterodimers of integrin from interacting with the collagen [28]. The results show that blocking CD44 did not affect 3D formation, whereas blocking integrin β1 significantly inhibited 3D formation when compared to the control group ($p < 0.0001$), presumably due to the loose packing of hASCs with CMG, indicating the inhibition of 3D formation (Fig. 3A, C). These data indicate that hASCs interact with CMG via integrin receptors to assemble into 3D constructs. The activation of integrin is known to induce FAK autophosphorylation, which then transmits signals to Ras homolog family member A (RhoA)/ROCK to phosphorylate myosin and cause the contraction of actin. To confirm that the assembly of our 3D constructs followed the same signaling pathway, we used inhibitors of FAK (PF-573228), ROCK (Y-27632), and myosin (blebbistatin) to determine whether 3D formation was inhibited. The results show that all three inhibitors inhibited 3D formation, as indicated by a significant increase in the size of the 3D constructs, particularly in the 1:4 group ($p < 0.0001$). This led to loosely packed 3D constructs, suggesting that the activation of integrin activates the FAK–ROCK–myosin signaling pathway to cause the contraction of actin, allowing hASCs to interact with and compact against CMG (Fig. 3B and C).

We hypothesized that, with an increasing cell:CMG ratio, more integrin receptors would be activated, as there would be more CMG near cells. Western blot analysis revealed a significant dose-dependent increase in the phosphorylation level of FAK ($p < 0.0001$) compared to the 1:0 group (Fig. 3D, Supp. Figs. S3D and E). As FAK is known to be involved in the suppression of anoikis, we examined the effect of blocking CD44 and integrin β1 on cell viability. Blocking CD44 did not affect cell viability while blocking integrin β1 resulted in a significant decrease in cell viability over 4 d when compared to the non-treated group ($p < 0.0001$). Taken together, our findings reveal that when hASCs are incubated with CMG, the binding of CMG to integrin receptors on the cell membranes activates integrin to phosphorylate FAK, which transmits signals to RhoA and ROCK, which then phosphorylate myosin to cause actin fiber contraction (Fig. 3F). Blocking integrin β1 or inhibition of FAK, ROCK, or myosin results in the inhibition of actin fiber contraction, resulting in the inhibition of 3D formation. Functionally blocked 3D constructs were loosely packed owing to the inhibition of 3D formation and had lower cell viability than the non-treated 3D constructs.

3.4. CMG improves the mass transfer and cell viability of 3D constructs

Microgel-assembled 3D constructs are known to be inherently porous in their microarchitectures. To determine the porosity of the 3D constructs formed with CMG, we performed a micro-CT scan. Our results indicated that the 1:0 group had no apparent pores within the structure, probably because of tight cell-to-cell and cell-to-ECM interaction. Pores became apparent in the 1:1 group and increased with increasing cell:

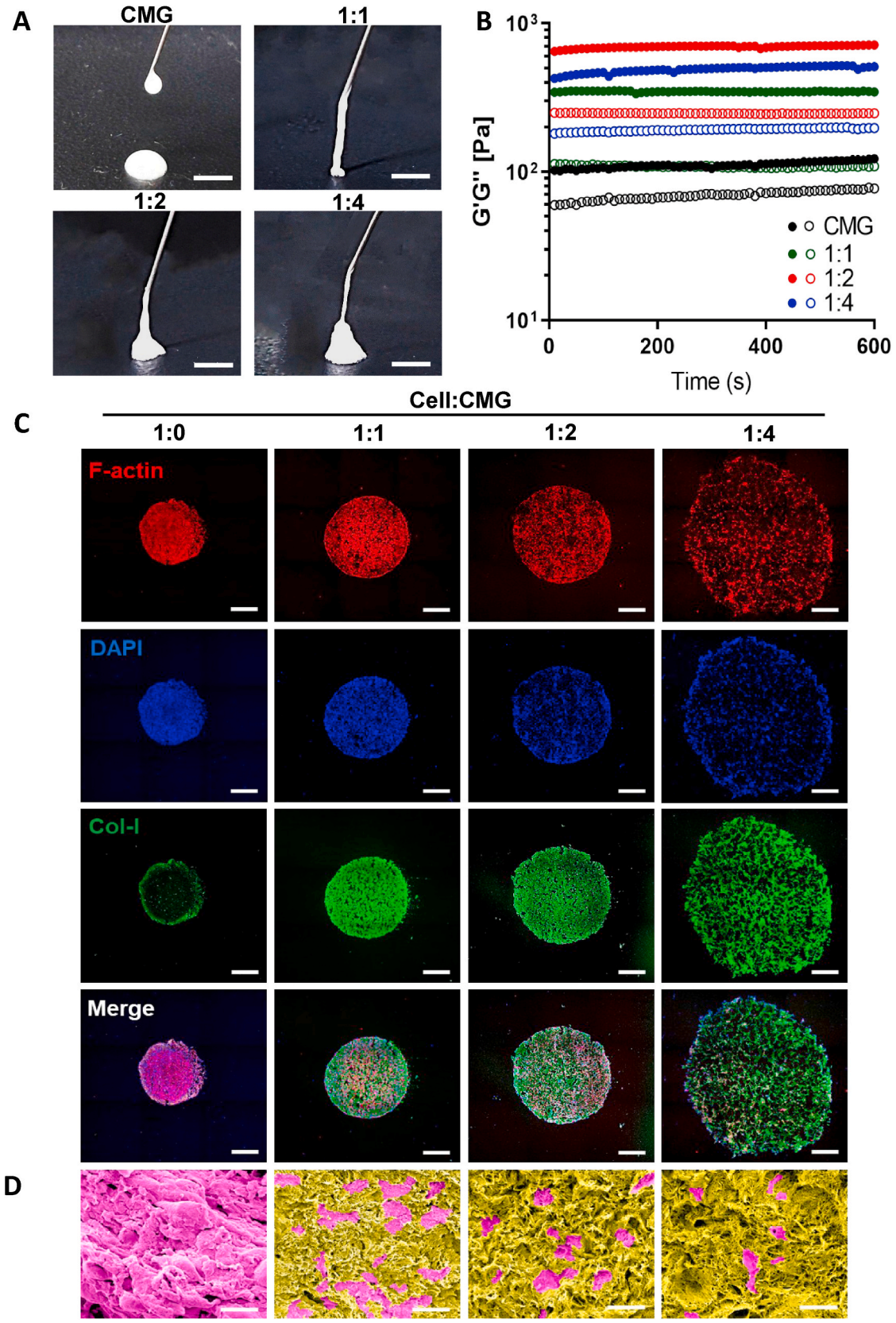

Fig. 2. Characterization of 3D constructs. (A) Photographic images showing injectability of CMG and 3D constructs prepared at 1:1, 1:2, and 1:4 ratios (2×10^5 hASCs/sample, cell:CMG ratio by pellet size) through a 24-gauge needle. Scale bar represents 5 mm. (B) Rheological properties showing storage (solid circle) and loss (open circle) moduli of CMG and 3D constructs. (C) Fluorescent images showing the distribution of cells and collagen type I inside 3D constructs. Images were captured under a confocal microscope. Nuclei were counterstained with DAPI. Scale bars represent 50 μm. (D) Colored SEM images showing the morphology of cells (pink) within the CMG network (yellow) of 3D constructs prepared at 1:0, 1:1, 1:2, or 1:4 ratios. The scale bar represents 20 μm.

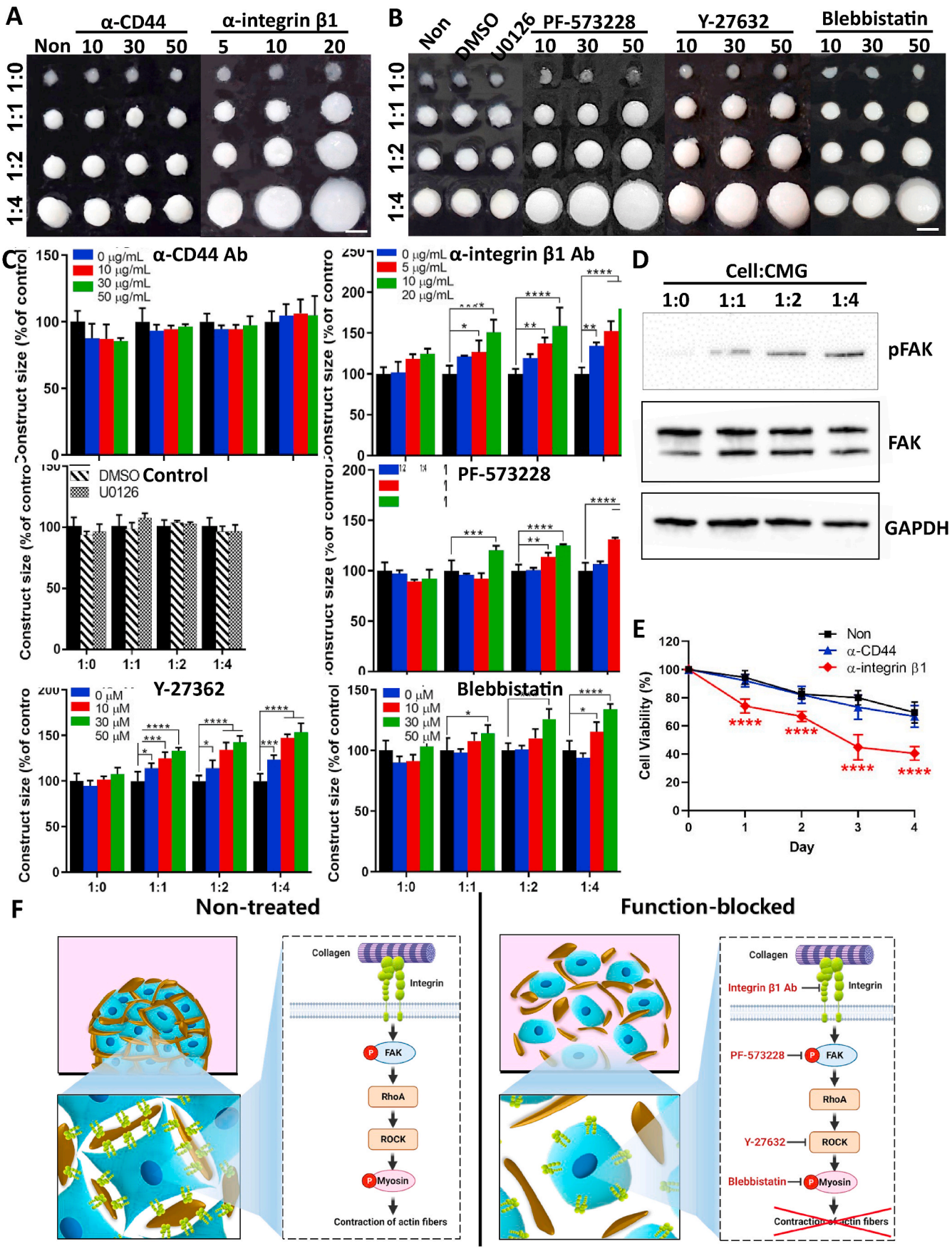

(caption on next page)

Fig. 3. Mechanism of CMG-hASCs assembly into 3D constructs. (A) Photographic images showing the effect of blocking CD44 or integrin β1 on the formation of 3D constructs. hASCs were treated with function-blocking antibodies against CD44 at 0, 10, 30, and 50 μg/mL or integrin β1 at 0, 5, 10, and 20 μg/mL for 30 min prior to incubation with hASCs. Scale bars represent 2 mm. (B) Photographic images showing the effect of chemical inhibitors on the formation of 3D constructs. DMSO and U0126 (ERK inhibitor) at 50 μM were included as the negative control. hASCs were treated with PF-573228 (FAK inhibitor), Y-27632 (ROCK inhibitor), or blebbistatin (myosin inhibitor) at 10, 30, or 50 μM. Scale bars represent 2 mm. (C) Quantification of the effect of function-blocking antibodies or chemical inhibitors on 3D construct size. n = 3 per group. (D) Immunoblot images showing phosphorylated FAK levels based on cell:CMG ratio (pellet size). GAPDH was used as a loading control. (E) Effect of function-blocking of CD44 or integrin β1 on cell viability as determined via trypan blue exclusion assay. n = 3 per group. (F) Schematic diagram illustrating 3D formation via assembly of cells with CMG through biological crosslinking with integrin and signaling pathway activation, and inhibition of 3D formation upon treatment with function-blocking antibodies or chemical inhibitors. All data are presented as mean ± SD. Two-way ANOVA with multiple comparison tests. *$p < 0.05$, **$p < 0.01$, ***$p < 0.001$, ****$p < 0.0001$ against the non-treated group.

CMG ratio (Fig. 4A). Quantification of the porosity revealed a significant increase from nearly 0 % porosity in the 1:0 group to approximately 40 % and 60 % in the 1:2 and 1:4 ratio groups, respectively ($p < 0.0001$; Fig. 4E). The porous microarchitecture within the 3D constructs would enhance mass transfer and promote the diffusion of nutrients and oxygen into the core. Incubation of the 3D constructs with the glucose analog 2-NBDG revealed that glucose could enter the core via diffusion in the 1:1, 1:2, and 1:4 groups, whereas only a limited amount of glucose reached the core of the 1:0 group, indicating limited diffusion (Fig. 4B). Under limited mass transfer, cells at the core of 3D constructs face glucose deprivation and hypoxia, which is reported to decrease their intracellular ATP levels [29]. Our results showed that intracellular ATP levels significantly increased in a dose-dependent manner with increasing cell:CMG ratio, which is consistent with the 2-NBDG immunofluorescent data ($p < 0.0001$) (Fig. 4F). The increased mass transfer would promote the diffusivity of oxygen into the core of the 3D constructs. To examine the absence of a hypoxic core, we stained 3D constructs with pimonidazole, a hypoxia marker. Immunofluorescent images of cross-sections of 3D constructs showed that the 1:0 group exhibited a hypoxic core, whereas, in the 1:1, 1:2, and 1:4 groups, hypoxic cells were scattered across the cross-section (Fig. 4C). To quantify the degree of hypoxia in the 3D constructs, western blotting was performed. As predicted, the 1:0 group was the most hypoxic, while the degree of hypoxia in the other experimental groups decreased with increasing cell:CMG ratio (Fig. 4G). In addition, it was anticipated that enhanced mass transfer would promote cell survival. Live and dead staining revealed that more dead cells were observed in the 1:0 group, while some dead cells were visible in the 1:1 and 1:2 groups, and nearly all the cells remained alive in the 1:4 group at d 7 (Fig. 4D). Consistent with LIVE/DEAD data, quantification of cell viability revealed that almost all cells were alive in d 1, with some cells in the 1:0 group beginning to die by d 3. Overall, a continuous decline in cell viability was observed over 28 d; however, a greater number of viable cells were observed in the 1:2 and 1:4 groups ($p < 0.0001$) at all time points compared to those in the 1:0 group (Fig. 4H). To determine the possible cause contributing to the decline in cell viability with increasing culture time, microCT scans were performed using the cells in the 1:4 group to measure changes in porosity throughout 21 d (Supp. Figs. S3F–G). The results suggested that as the culture time increased, the overall size of the 1:4 group decreased continuously due to cell contraction. This was accompanied by a progressive reduction in the microporosity within the microstructure, which may have ultimately caused cell death. Taken together, our data suggest that increasing the cell:CMG ratio allows cells to be viable for a longer duration.

3.5. CMG enhances the angiogenic potential of 3D constructs

To uncover the biological pathways enriched in 3D constructs, we performed mRNA sequencing analysis. DAVID analysis was performed on differentially expressed genes with a >1.5 fold change and a $p < 0.05$. It revealed that biological processes and genes involved in actin contraction, mass transfer, anti-apoptosis, and angiogenesis were enriched in the 1:4 group compared to the 1:0 group (Fig. 5A, Supp. Fig. S4A). Enrichment in actin contraction and mass transfer was as expected, as our previous function-blocking assay demonstrated that assembly into 3D constructs via activation of FAK-ROCK-myosin signaling pathway and analysis on the porosity of 3D constructs showed an increase in porosity along with concomitant enhancement in mass transfer. Analysis of the mRNA and protein levels of angiogenic factors, vascular endothelial growth factor (VEGF) and interleukin-8 (IL-8), and an anti-apoptotic factor, tissue inhibitor matrix metalloproteinase 1 (TIMP1), revealed that increasing the cell:CMG ratio increased the mRNA and protein levels of VEGF, IL-8, and TIMP1 (Fig. 5B–G). Additionally, to investigate on the effect of linear and significant decrease in cell viability as observed in Fig. 4H on the protein levels of VEGF, IL-8 and TIMP1, we quantified secretion of growth factors and determined that the protein levels of VEGF, IL-8, and TIMP1 decreased with culture time, in accordance with decreasing cell viability (Supp. Figs. S4B–D).

To assess angiogenic potential *in vitro*, we co-cultured 3D constructs prepared at 1:0, 1:1, 1:2, and 1:4 ratios and measured the formation of capillary-like tubular structures. Increasing the cell:CMG ratio significantly increased the capillary-like tube formation in HUVECs in a dose-dependent manner, as indicated by the increasing percentage of total tube length, from approximately 50 % in the 1:0 group to 100 % in the 1:4 group ($p < 0.0001$) (Fig. 6A and B). Co-culturing with CMG alone did not induce angiogenesis, as evidenced by the low degree of tube formation in the HUVECs. This indicated that co-culturing with CMG alone in a transwell was incapable of inducing angiogenesis. To further evaluate the angiogenic potential of the 3D constructs, each group was co-cultured with 1-mm-thick aortic rings collected from mice. To confirm that sprouting originated from endothelial cells and not from other supporting cells, the aortic rings were fixed and stained with an endothelial cell marker, lectin-IB4. Our results show that culturing aortic rings in EBM or with CMG hardly produced any microvessel sprouting from the aortic rings, presumably owing to the absence of angiogenic factors. Increasing the cell:CMG ratio from 1:0 to 1:4 significantly increased the degree of microvessel sprouting (from approximately 10%–70 %, respectively), with the 1:4 group exhibiting the most microvessel sprouting ($p < 0.0001$) (Fig. 6C and D). Taken together, our *in vitro* and *ex vivo* results show that increasing the cell:CMG ratio increases the angiogenic potential of 3D constructs. We propose that the dose-dependent increase in capillary-like tube formation of HUVECs and microvessel sprouting from aortic rings with increasing the cell:CMG ratio might be explained by increased secretion of angiogenic factors with increasing cell:CMG ratio.

3.6. CMG enhances the therapeutic effect of 3D constructs in a CLI model

We investigated the therapeutic effect of the 1:4 group in a mouse CLI model because it had the highest angiogenic potential *in vitro* and *ex vivo*. PBS, CMG, CMG/hASCs suspension, cell aggregates (1:0 group), or CMG-hASCs construct (1:4 group) were injected into the ischemic limbs 1 d after inducing ischemia, and their morphology and blood perfusion were monitored using laser Doppler imaging (Fig. 7A). At 28 d, injecting the CMG/hASCs suspension increased blood flow by approximately 40 % compared to the contralateral limb (Fig. 7B), resulting in the salvage of 20 % of ischemic limbs (Fig. 7C), whereas the cell aggregate and CMG groups showed a blood perfusion ratio that was not significantly different from that of the PBS group and rarely salvaged the ischemic

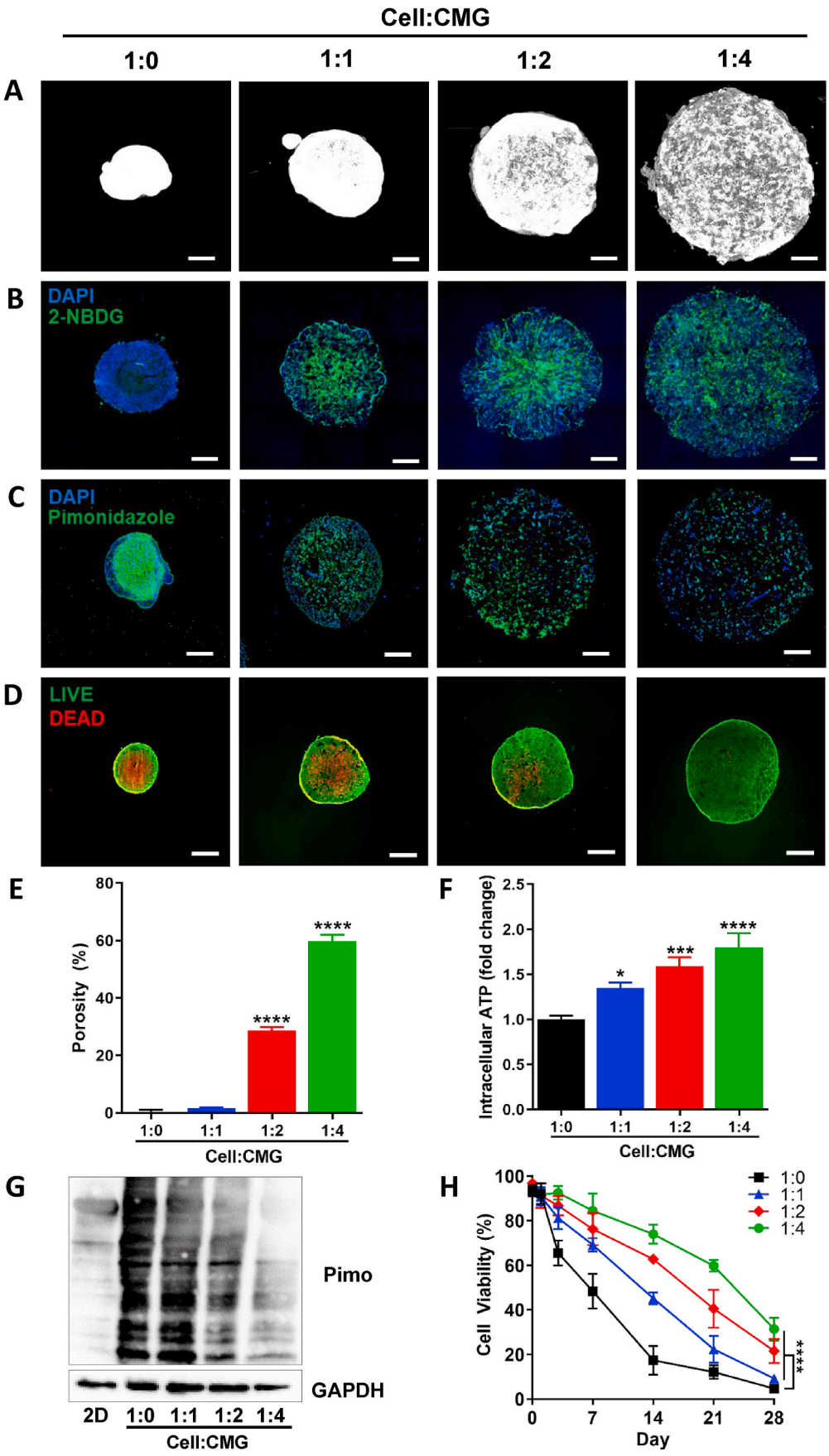

(caption on next page)

Fig. 4. Effect of CMG on the microstructure of 3D constructs. (A) Micro-CT visualization of a cross-section of 3D constructs prepared at 1:0, 1:1, 1:2, and 1:4 ratios (cell:CMG, pellet size) after incubating CMG with 2×10^5 hASCs for 24 h. Void spaces within the 3D constructs are depicted in gray color, and cells or CMG in white color. (B) Fluorescent images showing cellular uptake of 2-NBD-glucose across the inner mass of the 3D constructs. (C) Fluorescent images stained against hypoxia marker, pimonidazole. 3D constructs were pre-treated with pimonidazole at 10 mM for 5 h. (D) Live/dead images of 3D constructs prepared at 1:0, 1:2, 1:2, or 1:4 ratios (2×10^5 hASCs/sample, cell:CMG ratio by pellet size) at 7 d. Scale bars in panel A–D represent 500 μm. (E) Quantification of porosity inside 3D constructs, as analyzed using CTAn software. n = 3 per group (F) Quantification of intracellular ATP level as determined using Cell Titer-Glo® kit. n = 3 per group (G) Western blotting of cell lysates prepared from hASCs cultured as a monolayer and as 3D constructs prepared at 1:0, 1:1, 1:2, and 1:4 ratios (cell:CMG, pellet size) and stained against pimonidazole antibody. All groups were pre-treated with pimonidazole at 10 mM for 5 h. GAPDH was used as a loading control. (H) Cell viability of 3D constructs prepared at 1:0, 1:1, 1:2, or 1:4 ratios (2×10^5 hASCs/sample, cell:CMG ratio by pellet size) over 28 d, as determined via trypan blue exclusion assay. n = 3 per group. All data are presented as mean ± SD. One-way or two-way ANOVA with multiple comparison tests. *p < 0.05, ***p < 0.001, ****p < 0.0001 against the 1:0 group.

limbs. The CMG-hASCs construct group had a 20 % higher blood perfusion ratio than the CMG/hASCs suspension group (Fig. 7B) and was able to salvage 60 % of the ischemic limbs (Fig. 7C). Taken together, these results indicate that the CMG-hASCs construct group displayed higher therapeutic effect than CMG/hASCs suspension and cell aggregate groups and suggest that CMG in CMG-hASCs construct might act positively on therapeutic efficacy.

To examine whether the degradation rate of CMG in the CMG-hASCs construct is related to the therapeutic effect, we performed an *in vitro* enzymatic biodegradation assay and tracked the biodegradation rate using an *in vivo* imaging system (IVIS). It was observed from an *in vitro* assay that the degradation rate of CMG in CMG-hASCs constructs prepared at 1:1, 1:2, and 1:4 was significantly slower than that of CMG alone (Supp. Fig. S6A), probably because CMG were more readily accessible to collagenase in the absence of hASCs to assemble CMG. The biodegradation rate of Atto-488-conjugated CMG was determined from an *in vivo* assay on ischemic limbs and normal limbs (Supp. Figs. S6B–E). The biodegradation rate of CMG was not different from that of collagen/HA gel, indicating that the degree of biodegradation via fragmentation of the gel was not different. The fluorescent signal in the CMG-hASCs construct group decreased more slowly than in the collagen/HA gel, CMG, and CMG/hASCs suspension groups, indicating a slower CMG degradation rate in CMG-hASCs construct group (Supp. Figs. S6B and D). However, the fluorescent signal gradually decreased at a similar rate in all groups over 3 weeks and completely disappeared 4 weeks after injection into the ischemic limb (Supp. Figs. S6C and E). Taken together, it was demonstrated that the CMG degradation in the CMG-hASCs construct was delayed because it was assembled with cells, and it was suggested that CMG can support cells at the transplant site, which could affect therapeutic efficacy. However, the delay was not observed in the ischemic hindlimb, presumably due to the accelerated degradation caused via robust immune response after ischemic surgery.

Additionally, to investigate the effect of the construct size of CMG-hASCs on cell survival and therapeutic efficacy, we prepared CMG-hASCs at a 1:4 ratio with 5×10^4, 10×10^4, 20×10^4, or 40×10^4 cells/CMG-hASCs construct, resulting in an overall size of the 3D construct of 2 mm, 2.5 mm, 3 mm, or 4.2 mm in diameter, respectively (Supp. Figs. S5A–B). Our results indicated that increasing CMG-hASCs size increased the secretion of VEGF, IL-8, and TIMP1 from the CMG-hASCs construct, with a concomitant decrease in cell viability (Supp. Figs. S5C–F). Injection of varying sizes of CMG-hASCs construct revealed that injecting 2.5 mm and 3 mm groups with 10×10^4 or 20×10^4 cells/CMG-hASCs construct, respectively, resulted in a significant increase in blood perfusion compared to the PBS-treated group at 7 d, suggesting 10×10^4 or 20×10^4 cells/CMG-hASCs construct as the optimal size for achieving therapeutic efficacy (Supp. Figs. S5G–H).

3.7. CMG enhances cell survival and the therapeutic effect of 3D constructs in CLI

Cell survival was evaluated *in vivo* via the human nuclear antigen (HNA) staining of ischemic muscles. HNA-positive cells were not apparent in the contralateral, PBS, or CMG group, as cells were not injected (Supp. Fig. S7A). HNA-positive cells were observed over 28 d in the CMG-hASCs construct group, indicating the long-term presence of transplanted cells until 28 d. However, in the CMG/hASCs suspension group and cell aggregates group (1:0 ratio), HNA-positive cells were only observed until 14 d (Fig. 8A). The relative number of HNA-positive cells in the CMG-hASCs construct group was significantly higher than that in the CMG/hASCs suspension and cell aggregates groups until 7 d ($p < 0.01$) and 14 d ($p < 0.05$), respectively (Fig. 8D). Taken together, CMG-hASCs construct group demonstrated superior cell delivery effect and supported long-term cell survival after injection than CMG/hASCs suspension or cell aggregates groups.

The muscle regenerative potential of the CMG-hASCs construct was assessed using laminin-stained cross-sections of thigh muscle and by counting the number of regenerating myofibers, which are characterized by a centralized nucleus. On 14 d, few centralized nuclei were observed in the CMG/hASCs suspension and cell aggregates groups. In contrast, the CMG-hASCs construct group showed a significant and dramatic increase in the number of centralized nuclei compared to the other two groups, indicating extensive regeneration of muscle fibers by 14 d ($p < 0.0001$). At 28 d, significantly more centralized nuclei were observed in the CMG/hASCs suspension and cell aggregates groups, indicating some muscle regeneration by 28 d ($p < 0.05$). However, the CMG-hASCs construct group showed a significant reduction in the number of centralized nuclei when compared to the CMG/hASCs suspension and cell aggregates groups, with substantial restoration in the muscle architecture ($p < 0.0001$), similar to the architecture observed in the contralateral group (Fig. 8B, E, Supp. Fig. S7B). Further histological analysis of ischemic thigh muscles revealed full restoration of muscle fibers by 28 d, while deteriorated muscle fibers and fibrosis were observed in PBS, CMG, or cell aggregates groups. Consistent with IF data, centralized nuclei were observed in the suspension group at 28 d, which was also accompanied by fibrosis, indicating an ongoing process of muscle fiber regeneration (Supp. Figs. S8A and B). Our findings suggest that, of the groups tested, the CMG-hASCs construct group displayed the highest muscle regenerative potential.

To assess the angiogenic potential of the CMG/hASCs construct, muscle tissues were stained with CD31, a marker of endothelial cells. CD31-positive cells were observed in all treatment groups starting on 14 d, with the CMG-hASCs construct group showing a significantly higher number of CD31-positive cells per mm^2 than CMG/hASCs suspension and cell aggregates groups ($p < 0.05$) (Fig. 8C, F). At 28 d, more CD31-positive cells were observed in all treatment groups than at 14 d; however, the CMG-hASCs construct group expressed a significantly higher number of CD31-positive cells than the other two groups ($p < 0.0001$). In contrast, only a few CD31-positive cells were observed in PBS and CMG groups on 14 d and 28 d (Supp. Fig. S7C). Taken together, these results suggest that of the groups tested, the CMG-hASCs construct group displayed the highest angiogenic potential.

4. Discussion

Cell assembling has attracted attention as a promising technology to enhance cell viability and functions in stem cell therapy [30,31]. A major advantage of MSCs as stem cell therapy is their ability to secrete angiogenic, anti-inflammatory, and anti-apoptotic factors to facilitate

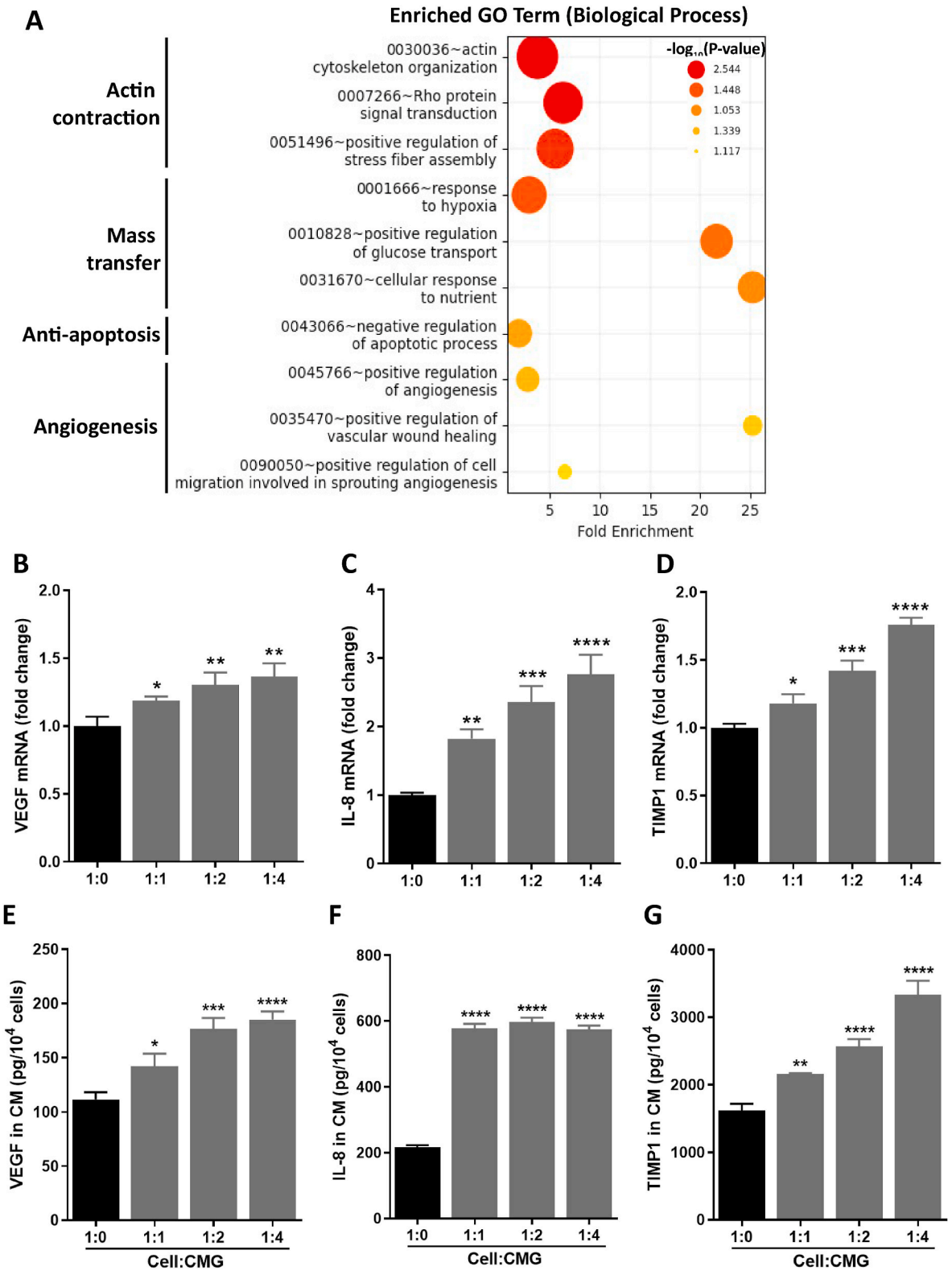

Fig. 5. Changes in gene expression of 3D constructs. (A) DAVID functional enrichment analysis via the biological process. Total mRNA was extracted from hASCs cultured on non-tissue culture plates and 3D constructs cultured with CMG at ratios of 1:0 and 1:4 for 24 h. Differentially expressed genes in the CMG-hASCs (1:4 ratio) group were selected based on genes with a >1.5 fold change and a p-value <0.05 against the cell aggregates (1:0 ratio) group. (B–D) Quantification of mRNA levels of VEGF (B), IL-8 (C), and TIMP1 (D) as prepared from 3D constructs prepared at 1:0, 1:1, 1:2 or 1:4 ratios (2×10^5 hASCs/sample, cell:CMG ratio by pellet size) via RT-PCR. (E–G) Quantification of protein levels of VEGF (E), IL-8 (F) and TIMP1 (G) in the conditioned medium by ELISA. n = 3 per group. All data are presented as mean ± SD. One-way ANOVA with multiple comparison tests. *p < 0.05, **p < 0.01, ***p < 0.001, ****p < 0.0001 against the 1:0 group.

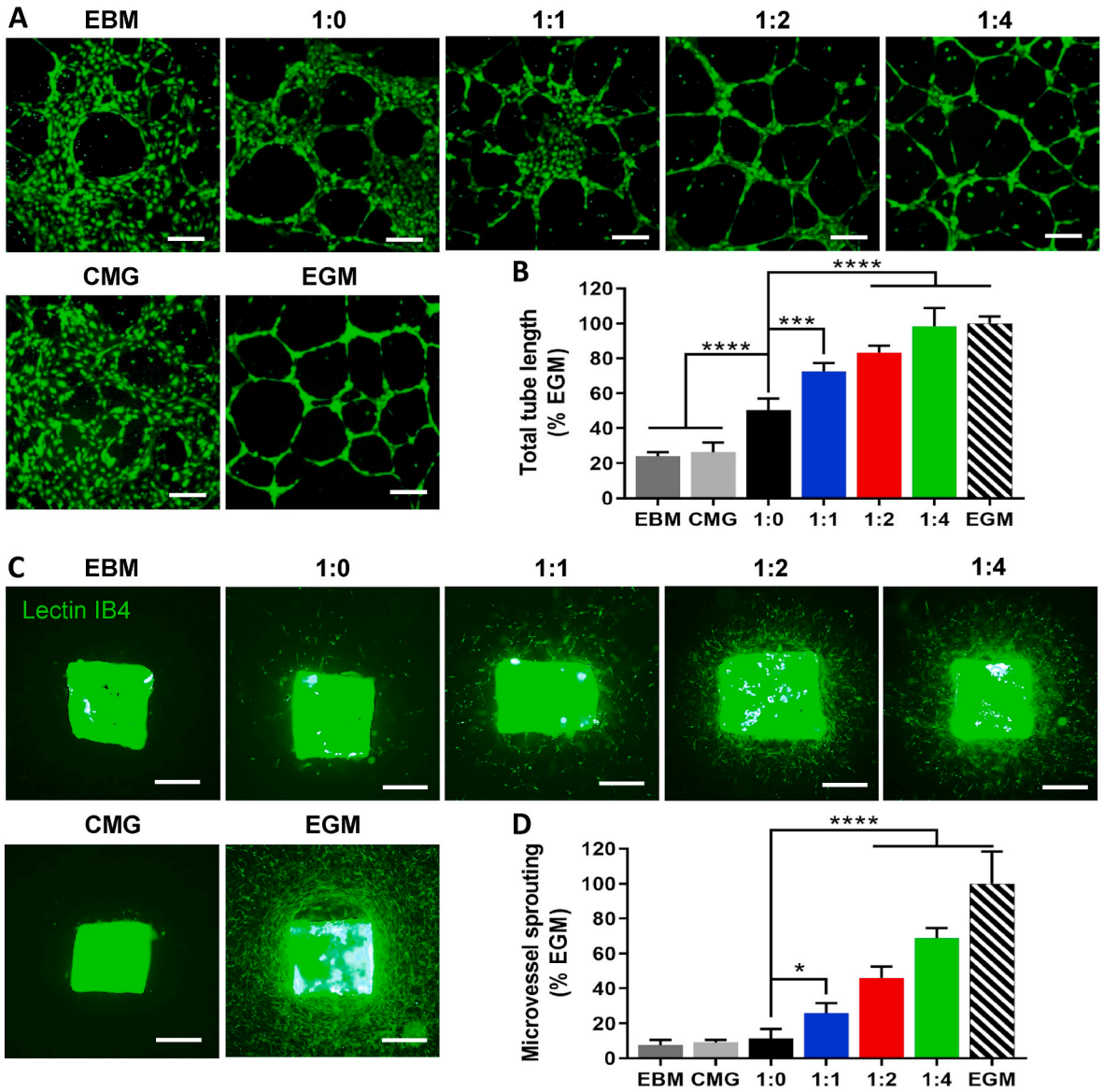

Fig. 6. Assessment of the angiogenic potential of 3D constructs *in vitro* and *ex vivo*. (A) Effect of co-culture of green fluorescent protein-tagged HUVECs with 3D constructs prepared at 1:0, 1:1, 1:2, or 1:4 ratios (2×10^5 hASCs/sample, cell:CMG ratio by pellet size) for 16 h on the tube formation. Endothelial basal media (EBM) and co-culture with CMG only were included as negative controls. Endothelial growth media (EGM: EBM + supplements) was included as a positive control. Scale bars represent 200 μm. (B) Effect of co-culture on the number of branching points of HUVECs. Data points were normalized against the value of the 1:0 group. n = 5 per group. (C) Effect of co-culture of aortic rings with 3D constructs prepared at 1:0, 1:1, 1:2, or 1:4 ratios for 7 d on microvessel sprouting. EBM and CMG were included as negative controls. EGM was included as a positive control. Scale bars represent 500 μm. (D) Quantification of microvessel sprouting in co-culture. Data points were normalized against the value of the 1:0 group. All data are presented as mean ± SD. One-way ANOVA with multiple comparison tests. *$p < 0.05$, ***$p < 0.001$, ****$p < 0.0001$ against the EBM group.

the regeneration of injured tissues. For the sustained release of paracrine factors, transplanted cells must remain viable; therefore, maintaining a high transplantation efficiency is essential for achieving high therapeutic efficacy. This study employed a collagen-based microgel, CMG, to assemble CMG-hASCs construct with a microporous microarchitecture that promoted mass transfer and cell-ECM contact, resulting in improved cell survival, angiogenic potential, and therapeutic efficacy.

CMG was manufactured via mechanical fragmentation of bulk hydrogel formed from atelocollagen and hyaluronic acid without chemical treatment. Atelocollagen is less antigenic and more biocompatible than natural collagen, and has a more flexible structure because of the absence of several cross-linked sites, resulting in greater solubility [32]. HA is an anionic polysaccharide chain that is also naturally found as an ECM component. We demonstrated that the addition of anionic HA to cationic atelocollagen results in the thinning of collagen fibers, enabling the fragmentation of collagen bulk hydrogels into microgels upon mechanical stress. These results are consistent with other studies that reported that positively charged collagen interacts with negatively charged HA to form a polyionic complex and that electrostatic interactions between collagen and HA molecules accelerate the nucleation and growth phases of collagen fibrillogenesis, resulting in thinner fibrils [33–36]. Xu et al. explained that this may be attributed to the strong hydrophilic properties of HA, as it is capable of absorbing water molecules to pull them away from the collagen monomers, strengthening intermolecular interactions between the collagen monomers and increasing the fibrillogenesis rate [37]. In contrast, several studies reported that the addition of HA to collagen gel did not accelerate fibrillogenesis [38–40]. These conflicting results may have resulted from variations, such as the concentration and molecular weight of HA, in the collagen–HA polyionic complex. In our results, when HA with a

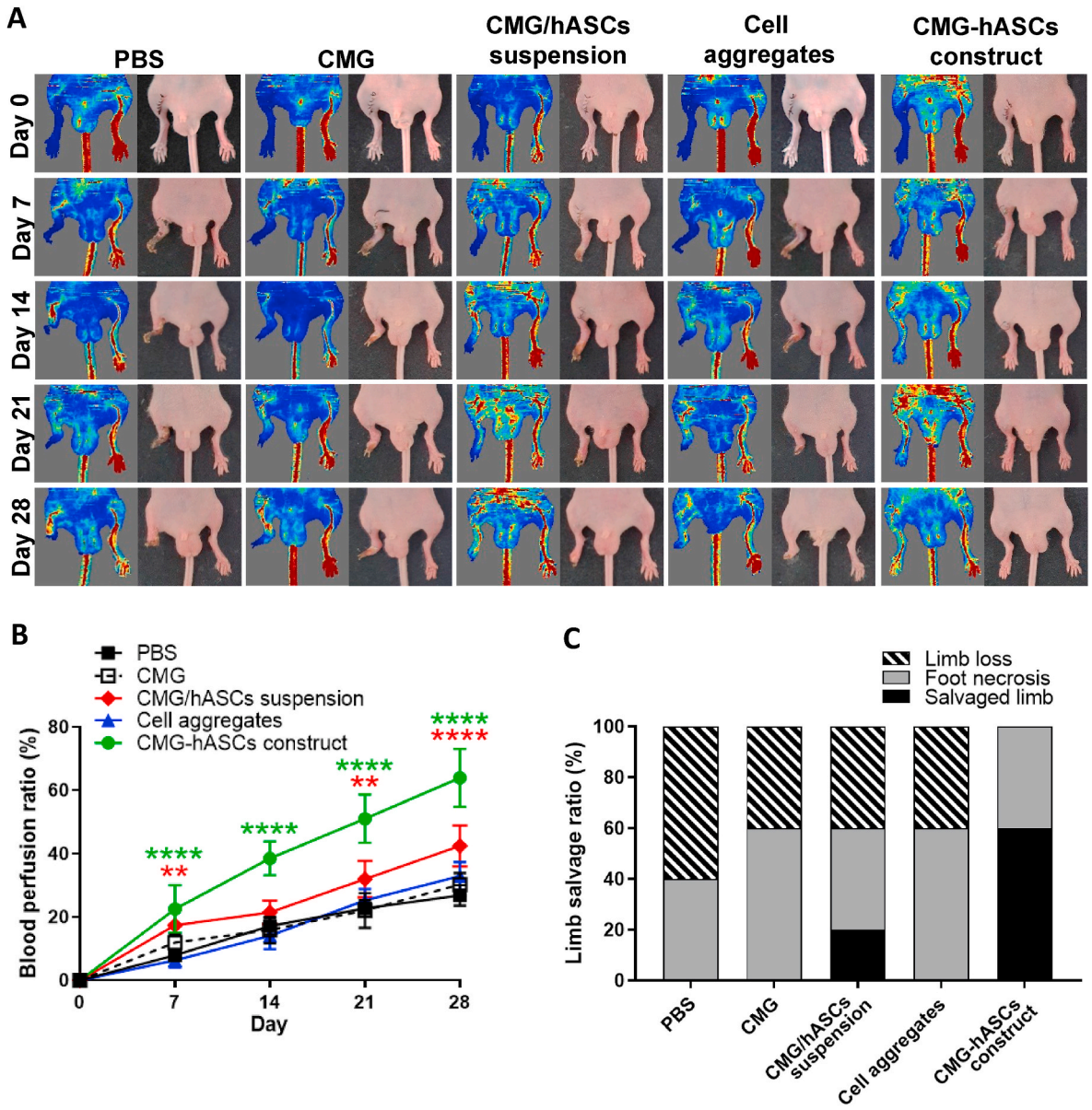

Fig. 7. Assessment of the angiogenic potential of 3D constructs in a CLI model. (A) Representative images of hindlimb morphology and blood perfusion in hindlimbs of a CLI mouse model over 28 d. Ischemia was induced in the left limb and 1 d after the surgery, the mice were treated with PBS, CMG, CMG/hASCs suspension (2×10^5 hASCs/mouse, hASCs and CMG in suspension, 1:4 ratio), cell aggregates (2×10^5 hASCs/mouse, 1:0 ratio), or CMG-hASCs construct (2×10^5 hASCs/mouse, 1:4 ratio) intramuscularly. n = 5 per group. (B) Quantification of blood perfusion ratio as determined from laser Doppler images. Blood perfusion was normalized against the normal limb. n = 5 per group. One-way ANOVA with multiple comparison tests. **p < 0.01, ****p < 0.0001 against PBS group. (C) Analysis of the physiological status of the ischemic limb as assessed on 28 d n = 6 per group.

molecular weight of approximately 300,000 Da was compared to HA with a molecular weight of 2,000,000 Da, CMG having a more uniform size distribution was obtained. Collagen is a major ECM component for cell adhesion and signaling via integrin receptors on the cell membrane [41]. We demonstrated that CMGs were involved in the formation of 3D constructs through integrin-mediated cell crosslinking. The function-blocking assay using antibodies and inhibitors revealed that the primary interaction between CMG and hASCs was mediated by the interactions between CMG and integrin receptors, which sequentially activated FAK, ROCK, and myosin to cause the contraction of actin fibers and form the 3D constructs (Fig. 3). The generated cellular traction force drew neighboring CMG toward the cells, allowing CMG to be packed into the 3D constructs. These findings are consistent with well-reported mechanotransduction pathways in which the binding of ECM activates integrin, which in turn autophosphorylates FAK. This transmits signals via the RhoA–ROCK cascade to directly phosphorylate the light myosin chain, inducing myosin to assemble with actin and other crosslinking proteins to form bundles of stress fibers [42,43]. The sliding of actin on myosin II generates a contractile force [42]. In addition to the contraction of actin fibers, FAK phosphorylation is known to regulate other important biological functions, including cell growth and survival [44]. Moreover, integrin-mediated phosphorylation of FAK is critical for preventing anoikis and promoting the survival of transplanted cells [45]. These findings indicate that increasing the cell:CMG ratio dose-dependently increased FAK phosphorylation and that blocking of integrin-β1 prevented hASCs from interacting with CMG and promoted cell death. Taken together, these results indicate that increasing the cell: CMG ratio activates the integrin-mediated outside-in signaling pathway to suppress anoikis and promote the long-term survival of cells.

The interaction between CMG and hASCs resulted in the enrichment

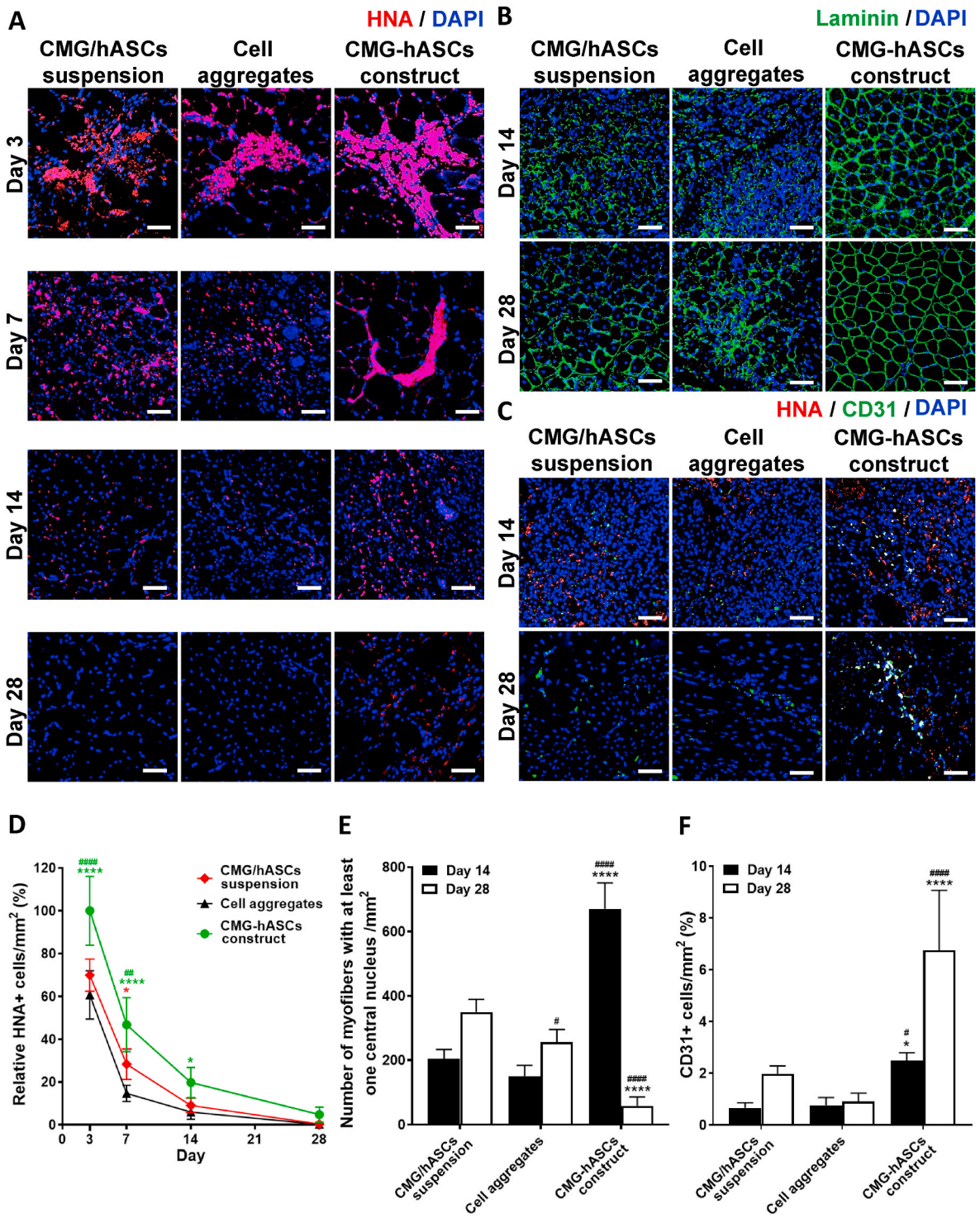

Fig. 8. Effect of CMG on survival and therapeutic effect in ischemic muscle. (A–C) Immunofluorescent images of ischemic thigh muscle stained against HNA (A), laminin (B), or CD31 and HNA (C), as collected from mice treated with CMG/hASCs suspension, cell aggregates, or CMG-hASCs construct (2×10^5 hASCs/mouse) over 28 d. Nuclei were counterstained against DAPI. Scale bars represent 50 μm. (D) Quantification of HNA-positive cells over 28 d. All data points are presented as relative values against the value of the CMG/hASCs suspension group. n = 5 per group. Two-way ANOVA with multiple comparison tests. *$p < 0.05$, ****$p < 0.0001$ against cell aggregates group. $^{\#\#}p < 0.01$, $^{\#\#\#\#}p < 0.0001$ against CMG/hASCs suspension group. (E) Quantification of the number of myofibers with at least one centralized nucleus per mm^2. All data are presented as mean ± SD. n = 5 per group (F) Quantification of CD31-positive cells in ischemic thigh muscle. All data are presented as mean ± SD. n = 5 per group. Two-way ANOVA with multiple comparison tests. *$p < 0.05$, ****$p < 0.0001$ against the cell aggregates group. $^{\#}p < 0.05$, $^{\#\#\#\#}p < 0.0001$ against CMG/hASCs suspension group.

of biological processes involved in anti-apoptosis and angiogenesis, which are key parameters required for CLI treatment. In *in vitro*, *ex vivo*, and *in vivo* models, our findings demonstrated that the CMG-hASCs construct possessed greater angiogenic potential than cell aggregates. The high trophic properties of hASCs, which release angiogenic factors such as vascular endothelial growth factor, basic fibroblast growth factor, and transforming growth factor-β in their secretome to augment the regeneration of injured tissue, are well-known [46,47]. Preconditioning cells in a hypoxic microenvironment upregulate the expression of angiogenic factors such as vascular endothelial growth factor, platelet-derived growth factor, and angiopoietin 1 [48]. Three-dimensional constructs, such as cell spheroids, induced intrinsic hypoxia and enhanced angiogenic potential and therapeutic efficacy in animal ischemic models [30,49,50]. In this study, increasing the cell: CMG ratio from 1:0 to 1:4 decreased the degree of hypoxia, probably due to enhanced mass transfer. We demonstrated that a dose-dependent increase in the cell:CMG ratio increased angiogenic potential in an *in vitro* tubularization assay and *ex vivo* aortic ring assay. Although the CMG-hASCs constructs exhibited less hypoxia than the cell aggregates (1:0 group), their angiogenic potential was higher than that of the cell aggregates. A possible explanation for the discrepancies may be due to differences in hypoxia-inducible factor-1α (HIF-1α) expression between acute and chronic hypoxia. HIF-1α is stabilized under acute hypoxia, whereas its expression is downregulated under chronic hypoxia [51]. TIMP1 is a key anti-apoptotic factor induced by HIF-1α in 3D cell spheroids, as previously reported [52]. TIMP1 was upregulated in CMG-hASCs constructs relative to cell aggregates, indicating that HIF-1α may have remained more stable in the CMG-hASCs construct. It is possible that cell aggregates exhibited chronic hypoxia due to the structural characteristics of its low porosity, whereas acute hypoxia was induced and angiogenic factors were upregulated in the CMG-hASCs constructs. Another possible explanation for the discrepancies may be that CMG directly activates hASCs in the constructs. Indeed, mRNA sequencing analysis supported that various factors including angiogenic factors, such as forkhead box C2, argonaute 2, and x-box binding protein 1, not related to hypoxia, were upregulated, indicating that culturing hASCs with CMG enhances the function of hASCs, resulting in the enrichment of biological processes involved in angiogenesis and the upregulation of genes involved in angiogenesis (Supp. Fig. S4A). ELISA analysis revealed that IL-8 was upregulated in the CMG-hASCs constructs relative to the cell aggregates group. We have previously reported that IL-8 is a crucial angiogenic factor upregulated via FGFR signaling, not hypoxia [30]. It is possible that CMG-activated integrin receptors increase the angiogenic potential of hASCs, or that endogenous factors secreted by the cells increase their angiogenic potential via autocrine and paracrine mechanisms.

Collagen or hASCs itself has been demonstrated to have angiogenic and therapeutic effects. Injection of collagen gel into the infarcted heart resulted in significantly higher levels of capillary formation and infiltration of myofibroblasts in the infarct area than in the saline group [53]. hASCs were able to secrete VEGF, hepatocyte growth factor, and transforming growth factor-β, demonstrating angiogenic and anti-apoptotic properties by increasing proliferation and decreasing apoptosis of endothelial cells and by increasing blood perfusion [4]. Therefore, it was necessary to determine if the unassembled mixture of CMG and hASCs could affect cell function. Since hASCs and CMG spontaneously assemble during incubation, cell functions such as angiogenic potential and cell survival could not be evaluated in *in vitro* experiments with or without assembly via CMG. The evaluation was verified in an *in vivo* experiment by comparing it with other experimental groups including the CMG-hASCs construct. Therapeutic effects, angiogenesis, and cell viability were better in the CMG/hASCs suspension group than the cell aggregates group, but not as good in the CMG-hASCs construct group (Figs. 7 and 8). The therapeutic variation between the CMG/hASCs suspension group and the CMG-hASCs construct group could potentially have been attributed to the disparity in the compactness of the transplanted cells. Condensation of hASCs has been reported to enhance their therapeutic potential [53]. A correlation was observed between the compactness of cells after injection and their therapeutic efficacy, with the condensed form exhibiting a greater degree of therapeutic efficacy than the spread form. As shown in Fig. 8, transplanted cells were observed as more condensed form with HNA-positive cells for a longer time in the CMG-hASCs construct compared to in the CMG/hASCs suspension and the cell aggregates groups. Biodegradation experiments revealed that the degradation rate of CMG was slower in the CMG-hASCs construct group than in the CMG alone or CMG/hASCs suspension groups (Supp. Fig. S6). VEGF was detected in the vicinity of the transplanted CMG-hASCs construct (Supp. Fig. S7D). From these results, it is speculated that the degradation rate of CMG would be lowered by assembling hASCs in the CMG-hASCs construct, which would slow the disaggregation of the cells, improve cell survival, and eventually positively affect the therapeutic efficacy. It is proposed that cell survival and therapeutic effect might be enhanced by controlling the biodegradation rate of CMG or disaggregation of assembled cells. The mechanism underlying the enhanced angiogenic potential of these CMG-hASCs constructs remains unclear. Future research is required to dissect the molecular mechanisms underlying the upregulation of key angiogenic factors and anti-apoptotic factors in the CMG-hASCs construct. The identification of the possible signaling pathways involved in this enhanced angiogenic potential will pave the way for breakthroughs in enhancing treatments for CLI.

Numerous studies demonstrated that injection of cell spheroids could rescue ischemic limb from necrosis and increase blood perfusion [49,54,55]. However, in this study, the therapeutic effects of the cell aggregates group were comparable to those of the PBS group. The discrepancy in the therapeutic effect of cell aggregates may have resulted from differences in transplanted cell numbers. Previous studies that demonstrated the therapeutic effects of cell spheroids in mouse ischemia models used doses ranging from 10^6 to 10^7 cells [49,54,55]. In contrast, 2×10^5 cells were injected into the ischemic hindlimb to evaluate the therapeutic effects in this study. Our results showed that CMG-hASCs construct could achieve sufficient therapeutic effects with 2×10^5 cells. This result proves the excellent therapeutic efficacy of the CMG-hASCs constructs in CLI. Although we could salvage ischemic limbs in the mouse CLI model by injecting CMG-hASCs and despite the improved yet linear decline in cell viability, this enhancement in survival rate may not be enough for translation to therapeutic effects in humans and successful clinical application. Further research is necessary to enhance the survival rate of transplanted cells, although our CMG platform demonstrated an improvement in cell survival rate. In addition, CMG-hASCs may need to be injected in a relatively large volume because CMG is added for cell assembly. Indeed, for successful clinical application in humans, it may be necessary to reduce the volume of vehicle required to inject CMG-hASCs, thereby reducing the total volume injected and providing more space for injecting higher cell doses.

5. Conclusion

In summary, we fabricated a CMG and used it as a micronized scaffold to deliver hASCs to the injury site. Because the collagen hydrogel itself is an extremely viscoelastic gel, HA was added to facilitate the fragmentation of the bulk collagen gel into a micro-sized gel. Assembly into CMG-hASCs construct occurs primarily through CMG binding to integrin receptors, acting on the FAK-ROCK-myosin signaling pathway, which finally induces the contraction of actin. CMG-hASCs construct had a porous microarchitecture that promoted mass transfer, with enhanced glucose uptake and a less hypoxic core, which promoted long-term cell viability. mRNA-seq analysis revealed that biological processes related to actin contraction, mass transfer, anti-apoptosis, and angiogenesis were enriched when compared with cell monolayer or 3D cell aggregates. We demonstrated that increasing the cell-to-CMG ratio also increased angiogenic potential *in vitro* and *ex vivo* in a dose-dependent

manner. Injecting the CMG-hASCs construct was shown to be a more therapeutically effective method of inducing angiogenesis than injecting as CMG/hASCs suspension of cell aggregates, as CMG-hASCs construct demonstrated increased cell survival, muscle regenerative potential, and angiogenic potential. Collectively, the CMG-hASCs construct not only demonstrated improved cell survival via enhanced mass transfer but also showed enhanced angiogenic potential to effectively treat CLI.

Ethics Approval

All procedures involving animals were approved by the International Animal Care and Use Committee of the Korea Institute of Science and Technology [KIST-2021-090]. The authors declare that all experiments involving animals were in compliance with the all relevant ethical regulations.

CRediT authorship contribution statement

Haeun Chung: Conceptualization, Formal analysis, Investigation, Methodology, Visualization, Writing – original draft, Writing – review & editing. **Jung-Kyun Choi:** Formal analysis, Methodology, Writing – review & editing. **Changgi Hong:** Methodology. **Youngseop Lee:** Formal analysis, Methodology. **Ki Hyun Hong:** Formal analysis, Methodology. **Seung Ja Oh:** Conceptualization, Supervision. **Jeongmin Kim:** Conceptualization, Supervision. **Soo-Chang Song:** Conceptualization, Supervision. **Jong-Wan Kim:** Formal analysis. **Sang-Heon Kim:** Conceptualization, Funding acquisition, Methodology, Project administration, Supervision, Writing – original draft, Writing – review & editing.

Declaration of competing interest

The authors declare that they have no conflicting financial interests or any other competing interests that could have influenced the data reported in this paper.

Acknowledgements

This research was supported by a grant from the Korean Fund for Regenerative Medicine, funded by the Ministry of Science and ICT, and the Ministry of Health & Welfare of Korea [22C0620L1-11]. The illustrations in the figures were created using BioRender.com.

Appendix A. Supplementary data

Supplementary data to this article can be found online at https://doi.org/10.1016/j.bioactmat.2023.12.008.

References

[1] L. Beltrán-Camacho, M. Rojas-Torres, M.C. Durán-Ruiz, Current status of angiogenic cell therapy and related strategies applied in critical limb ischemia, Int. J. Mol. Sci. 22 (2021) 1–27, https://doi.org/10.3390/ijms22052335.
[2] M. Hassanshahi, S. Khabbazi, Y. Peymanfar, A. Hassanshahi, Z. Hosseini-Khah, Y. W. Su, C.J. Xian, Critical limb ischemia: current and novel therapeutic strategies, J. Cell. Physiol. 234 (2019) 14445–14459, https://doi.org/10.1002/jcp.28141.
[3] M. Mousaei Ghasroldasht, J. Seok, H.S. Park, F.B. Liakath Ali, A. Al-Hendy, Stem cell therapy: from idea to clinical practice, Int. J. Mol. Sci. 23 (2022) 2850, https://doi.org/10.3390/ijms23052850.
[4] J. Rehman, D. Traktuev, J. Li, S. Merfeld-Clauss, C.J. Temm-Grove, J.E. Bovenkerk, C.L. Pell, B.H. Johnstone, R.V. Considine, K.L. March, Secretion of angiogenic and Antiapoptotic factors by human adipose stromal cells, Circulation 109 (2004) 1292–1298, https://doi.org/10.1161/01.CIR.0000121425.42966.F1.
[5] S. Baldari, G. Di Rocco, M. Piccoli, M. Pozzobon, M. Muraca, G. Toietta, Challenges and strategies for improving the regenerative effects of mesenchymal stromal cell-based therapies, Int. J. Mol. Sci. 18 (2017) 2087, https://doi.org/10.3390/ijms18102087.
[6] Y. Xu, T. Shi, A. Xu, L. Zhang, 3D spheroid culture enhances survival and therapeutic capacities of MSCs injected into ischemic kidney, J. Cell Mol. Med. 20 (2016) 1203–1213, https://doi.org/10.1111/jcmm.12651.
[7] Y. Petrenko, E Syková, Š. Kubinová, The therapeutic potential of three-dimensional multipotent mesenchymal stromal cell spheroids, Stem Cell Res. Ther. 8 (2017) 94, https://doi.org/10.1186/s13287-017-0558-6.
[8] C. Rathnam, L. Yang, S. Castro-Pedrido, J. Luo, L. Cai, K.-B. Lee, Hybrid SMART spheroids to enhance stem cell therapy for CNS injuries, Sci. Adv. 7 (2021), eabj2281, https://doi.org/10.1126/sciadv.abj2281.
[9] G. Choe, J. Park, H. Park, J.Y. Lee, Hydrogel biomaterials for stem cell microencapsulation, Polymers 10 (2018) 997, https://doi.org/10.3390/polym10090997.
[10] A. Marchini, F. Gelain, Synthetic scaffolds for 3D cell cultures and organoids: applications in regenerative medicine, Crit. Rev. Biotechnol. 42 (2022) 468–486, https://doi.org/10.1080/07388551.2021.1932716.
[11] S. Lee, E. Choi, M.J. Cha, K.C. Hwang, Cell adhesion and long-term survival of transplanted mesenchymal stem cells: a prerequisite for cell therapy, Oxid. Med. Cell. Longev. 2015 (2015) 632902, https://doi.org/10.1155/2015/632902.
[12] A. Ovsianikov, A. Khademhosseini, V. Mironov, The Synergy of scaffold-based and scaffold-free tissue engineering strategies, Trends Biotechnol. 36 (2018) 348–357, https://doi.org/10.1016/j.tibtech.2018.01.005.
[13] Q. Feng, D. Li, Q. Li, S. Li, H. Huang, H. Li, H. Dong, X. Cao, Dynamic nanocomposite microgel assembly with microporosity, injectability, tissue-adhesion, and sustained drug release promotes articular cartilage repair and regeneration, Adv. Healthc. Mater. 11 (2022), e2102395, https://doi.org/10.1002/adhm.202102395.
[14] Q. Feng, D. Li, Q. Li, X. Cao, H. Dong, Microgel assembly: fabrication, characteristics and application in tissue engineering and regenerative medicine, Bioact. Mater. 9 (2022) 105–119, https://doi.org/10.1016/j.bioactmat.2021.07.020.
[15] S. Xin, O.M. Wyman, D.L. Alge, Assembly of PEG microgels into porous cell-instructive 3D scaffolds via thiol-ene click chemistry, Adv. Healthc. Mater. 7 (2018), e1800160, https://doi.org/10.1002/adhm.201800160.
[16] M. Barisam, M.S. Saidi, N. Kashaninejad, N.T. Nguyen, Prediction of necrotic core and hypoxic zone of multicellular spheroids in a microbioreactor with a U-shaped barrier, Micromachines 9 (2018) 94, https://doi.org/10.3390/mi9030094.
[17] K. Wang, Z. Wang, H. Hu, C. Gao, Supramolecular microgels/microgel scaffolds for tissue repair and regeneration, Supramolecular Materials 1 (2022), 100006, https://doi.org/10.1016/j.supmat.2021.100006.
[18] C.M. Dumont, M.A. Carlson, M.K. Munsell, A.J. Ciciriello, K. Strnadova, J. Park, B. J. Cummings, A.J. Anderson, L.D. Shea, Aligned hydrogel tubes guide regeneration following spinal cord injury, Acta Biomater. 86 (2019) 312–322, https://doi.org/10.1016/j.actbio.2018.12.052.
[19] N.F. Truong, E. Kurt, N. Tahmizyan, S.C. Lesher-Pérez, M. Chen, N.J. Darling, W. Xi, T. Segura, Microporous annealed particle hydrogel stiffness, void space size, and adhesion properties impact cell proliferation, cell spreading, and gene transfer, Acta Biomater. 94 (2019) 160–172, https://doi.org/10.1016/j.actbio.2019.02.054.
[20] C.B. Highley, K.H. Song, A.C. Daly, J.A. Burdick, Jammed microgel inks for 3D printing applications, Adv. Sci. 6 (2019), 1801076, https://doi.org/10.1002/advs.201801076.
[21] O. Jeon, Y.B. Lee, T.J. Hinton, A.W. Feinberg, E. Alsberg, Cryopreserved cell-laden alginate microgel bioink for 3D bioprinting of living tissues, Mater. Today Chem. 12 (2019) 61–70, https://doi.org/10.1016/j.mtchem.2018.11.009.
[22] S. Xin, O.M. Wyman, D.L. Alge, Assembly of PEG microgels into porous cell-instructive 3D scaffolds via thiol-ene click chemistry, Adv. Healthc. Mater. 7 (2018), e1800160, https://doi.org/10.1002/adhm.201800160.
[23] K. Cockerham, V.J. Hsu, Collagen-based dermal fillers: Past, present, future, Facial Plast. Surg. 25 (2009) 106–113, https://doi.org/10.1055/s-0029-1220650.
[24] Y. Li, W. Liu, F. Liu, Y. Zeng, S. Zuo, S. Feng, C. Qi, B. Wang, X. Yan, A. Khademhosseini, J. Bai, Y. Du, Primed 3D injectable microniches enabling low-dosage cell therapy for critical limb ischemia, Proc Natl Acad Sci U S A 111 (2014) 13511–13516, https://doi.org/10.1073/pnas.1411295111.
[25] D. Thomas, G. Marsico, I. Liza, M. Isa, A. Thirumaran, X. Chen, B. Lukasz, G. Fontana, B. Rodriguez, M. Marchetti-Deschmann, T. O'brien, A. Pandit, Temporal changes guided by mesenchymal stem cells on a 3D microgel platform enhance angiogenesis in vivo at a low-cell dose, Proc Natl Acad Sci U S A 117 (2020) 19033–19044, https://doi.org/10.1073/pnas.2008245117/-/DCSupplemental.
[26] Y. Yang, F.M.V. Rossi, E.E. Putnins, Ex vivo expansion of rat bone marrow mesenchymal stromal cells on microcarrier beads in spin culture, Biomaterials 28 (2007) 3110–3120, https://doi.org/10.1016/j.biomaterials.2007.03.015.
[27] Y. Lee, Y. Lee, M. Lee, D. Koo, D. Kim, H. Kim, K. Lee, J. Kim, STORM imaging buffer with a refractive index matched to standard immersion oil, ACS Photonics 10 (2023), 2589-2597, doi:10.1021/acsphotonics.3c00806.
[28] I. Boraschi-Diaz, J. Wang, J.S. Mort, S.v. Komarova, Collagen type i as a ligand for receptor-mediated signaling, Front Phys 5 (2017), https://doi.org/10.3389/fphy.2017.00012.
[29] A. Moya, J. Paquet, M. Deschepper, N. Larochette, K. Oudina, C. Denoeud, M. Bensidhoum, D. Logeart-Avramoglou, H. Petite, Human mesenchymal stem cell failure to Adapt to glucose shortage and rapidly Use intracellular Energy Reserves through Glycolysis Explains poor cell survival after implantation, Stem Cell. 36 (2018) 363–376, https://doi.org/10.1002/stem.2763.
[30] J. Choi, W. Choi, Y. Joo, H. Chung, D. Kim, S.J. Oh, S.H. Kim, FGF2-primed 3D spheroids producing IL-8 promote therapeutic angiogenesis in murine hindlimb ischemia, NPJ Regen Med 6 (2021) 48, doi:10.1038/s41536-021-00159-7.
[31] N.H. Lee, O. Bayaraa, Z. Zechu, H.S. Kim, Biomaterials-assisted spheroid engineering for regenerative therapy, BMB Rep 54 (2021) 356–367, https://doi.org/10.5483/BMBRep.2021.54.7.059.

[32] J. Lee, S.J. Oh, S.H. An, W.D. Kim, S.H. Kim, Machine learning-based design strategy for 3D printable bioink: elastic modulus and yield stress determine printability, Biofabrication 12 (2020) 035018, doi:10.1088/1758-5090/ab8707.
[33] T. Taguchi, T. Ikoma, J. Tanaka, An improved method to prepare hyaluronic acid and type II collagen composite matrices, J. Biomed. Mater. Res. 61 (2002) 330–336, https://doi.org/10.1002/jbm.10147.
[34] S. Chen, Q. Zhang, T. Nakamoto, N. Kawazoe, G. Chen, Highly active porous scaffolds of collagen and hyaluronic acid prepared by suppression of polyion complex formation, J. Mater. Chem. B 2 (2014) 5612–5619, https://doi.org/10.1039/c4tb00780h.
[35] J.E. Scott, Proteoglycan-fibrillar collagen interactions, Biochem. J. 252 (1988) 313–323, https://doi.org/10.1042/bj2520313.
[36] S.W. Tsai, R.L. Liu, F.Y. Hsu, C.C. Chen, A study of the influence of polysaccharides on collagen self-assembly: nanostructure and kinetics, Biopolymers 83 (2006) 381–388, https://doi.org/10.1002/bip.
[37] Q. Xu, J.E. Torres, M. Hakim, P.M. Babiak, P. Pal, C.M. Battistoni, M. Nguyen, A. Panitch, L. Solorio, J.C. Liu, Collagen- and hyaluronic acid-based hydrogels and their biomedical applications, Mater. Sci. Eng. R Rep. 146 (2021) 100641, https://doi.org/10.1016/j.mser.2021.100641.
[38] S.T. Kreger, S.L. Voytik-Harbin, Hyaluronan concentration within a 3D collagen matrix modulates matrix viscoelasticity, but not fibroblast response, Matrix Biol. 28 (2009) 336–346, https://doi.org/10.1016/j.matbio.2009.05.001.
[39] S.M. Kuo, Y.J. Wang, G.C.C. Niu, H.E. Lu, S.J. Chang, Influences of hyaluronan on type II collagen fibrillogenesis in vitro, J. Mater. Sci. Mater. Med. 19 (2008) 1235–1241, https://doi.org/10.1007/s10856-007-3205-4.
[40] X. Xin, A. Borzacchiello, P.A. Netti, L. Ambrosio, L. Nicolais, Hyaluronic-acid-based semi-interpenetrating materials, J. Biomater. Sci. Polym. Ed. 15 (2004) 1223–1236, https://doi.org/10.1163/1568562041753025.
[41] J. Elango, C. Hou, B. Bao, S. Wang, J.E. Maté Sánchez de Val, W. Wenhui, The molecular interaction of collagen with cell receptors for biological function, Polymers 14 (2022) 876, https://doi.org/10.3390/polym14050876.
[42] F. Martino, A.R. Perestrelo, V. Vinarský, S. Pagliari, G. Forte, Cellular mechanotransduction: from tension to function, Front. Physiol. 9 (2018) 824, https://doi.org/10.3389/fphys.2018.00824.
[43] B. Cheng, M. Lin, G. Huang, Y. Li, B. Ji, G.M. Genin, V.S. Deshpande, T.J. Lu, F. Xu, Cellular mechanosensing of the biophysical microenvironment: a review of mathematical models of biophysical regulation of cell responses, Phys. Life Rev. 22–23 (2017) 88–119, https://doi.org/10.1016/j.plrev.2017.06.016.
[44] S.-T. Lim, X.L. Chen, Y. Lim, D.A. Hanson, T.-T. Vo, K. Howerton, N. Larocque, S. J. Fisher, D.D. Schlaepfer, D. Ilic, Nuclear FAK promotes cell proliferation and survival through FERM-enhanced p53 degradation, Mol. Cell 29 (2008) 9–22, https://doi.org/10.1016/j.molcel.2007.11.031.
[45] J. Alanko, A. Mai, G. Jacquemet, K. Schauer, R. Kaukonen, M. Saari, B. Goud, J. Ivaska, Integrin endosomal signalling suppresses anoikis, Nat. Cell Biol. 17 (2015) 1412–1421, https://doi.org/10.1038/ncb3250.
[46] X. Li, T. Ma, J. Sun, M. Shen, X. Xue, Y. Chen, Z. Zhang, Harnessing the secretome of adipose-derived stem cells in the treatment of ischemic heart diseases, Stem Cell Res. Ther. 10 (2019) 196, doi:10.1186/s13287-019-1289-7.
[47] A. Trzyna, A. Banaś-Ząbczyk, Adipose-derived stem cells secretome and its potential application in "stem cell-free therapy, Biomolecules 11 (2021) 878, https://doi.org/10.3390/biom11060878.
[48] T. Hashimoto, F. Shibasaki, Hypoxia-inducible factor as an angiogenic master switch, Front. Pediatr. 3 (2015) 33, doi:10.3389/fped.2015.00033.
[49] S.H. Bhang, S.W. Cho, W.G. La, T.J. Lee, H.S. Yang, A.Y. Sun, S.H. Baek, J.W. Rhie, B.S. Kim, Angiogenesis in ischemic tissue produced by spheroid grafting of human adipose-derived stromal cells, Biomaterials 32 (2011) 2734–2747, https://doi.org/10.1016/j.biomaterials.2010.12.035.
[50] R. Zhang, W. Luo, Y. Zhang, D. Zhu, A.C. Midgley, H. Song, A. Khalique, H. Zhang, J. Zhuang, D. Kong, X. Huang, Particle-based artificial three-dimensional stem cell spheroids for revascularization of ischemic diseases, Sci. Adv. 6 (2020) 1–14, https://doi.org/10.1126/sciadv.aaz8011.
[51] K. Saxena, M.K. Jolly, Acute vs. chronic vs. cyclic hypoxia: their differential dynamics, molecular mechanisms, and effects on tumor progression, Biomolecules 9 (2019) 339, https://doi.org/10.3390/biom9080339.
[52] J. Choi, H. Chung, S. Ja, J. Kim, S. Kim, Functionally enhanced cell spheroids for stem cell therapy: Role of TIMP1 in the survival and therapeutic effectiveness of stem cell spheroids, Acta Biomater. 166 (2023) 454–469, https://doi.org/10.1016/j.actbio.2023.05.033.
[53] N.F. Huang, J.Y. Yu, R. Sievers, S. Li, R.J. Lee, Injectable biopolymers enhance angiogenesis after myocardial infarction, Tissue Eng. 11 (2005) 1860 –1866 doi: 10.1089/ten.2005.11.1860.
[54] S. Lim, H.Y. Yoon, S.J. Park, S. Song, M.K. Shim, S. Yang, S.W. Kang, D.K. Lim, B. S. Kim, S.H. Moon, K. Kim, Predicting in vivo therapeutic efficacy of bioorthogonally labeled endothelial progenitor cells in hind limb ischemia models via non-invasive fluorescence molecular tomography, Biomaterials 266 (2021), 120472, https://doi.org/10.1016/j.biomaterials.2020.120472.
[55] I.S. Park, P.S. Chung, J.C. Ahn, Enhanced angiogenic effect of adipose-derived stromal cell spheroid with low-level light therapy in hind limb ischemia mice, Biomaterials 35 (2014) 9280–9289, https://doi.org/10.1016/j.biomaterials.2014.07.061.